Scalings for eddy buoyancy transfer across continental slopes under retrograde winds

Yan Wang[a], and Andrew L. Stewart[b]

[a]*Department of Ocean Science and Hong Kong Branch of Southern Marine Science & Engineering Guangdong Laboratory, The Hong Kong University of Science and Technology, Hong Kong, China*
[b]*Department of Atmospheric and Oceanic Sciences, University of California, Los Angeles, CA 90095, USA*

Abstract

Baroclinic eddy restratification strongly influences the ocean's general circulation and tracer budgets, and has been routinely parameterized via the Gent-McWilliams (GM) scheme in coarse-resolution ocean climate models. These parameterizations have been improved via refinements of the GM eddy transfer coefficient using eddy-resolving simulations and theoretical developments. However, previous efforts have focused primarily on the open ocean, and the applicability of existing GM parameterization approaches to continental slopes remains to be addressed. In this study, we use a suite of eddy-resolving, process-oriented simulations to test scaling relationships between eddy buoyancy diffusivity, mean flow properties, and topographic geometries in simulations of baroclinic turbulence over continental slopes. We focus on the case of retrograde (i.e., opposing the direction of topographic wave propagation) winds, a configuration that arises commonly around the margins of the subtropical gyres.

Three types of scalings are examined, namely, the GEOMETRIC framework developed by Marshall et al. (2012) [A framework for parameterizing eddy potential vorticity fluxes. J. Phys. Oceanogr. 42, 539-557], a new "Cross-Front" (CF) scaling derived via dimensional arguments, and the mixing length theory (MLT)-based scalings tested recently by Jansen et al. (2015) [Parameterization of eddy fluxes based on a mesoscale energy budget. Ocean Model. 92, 28-41] over a flat ocean bed. The present study emphasizes the crucial role of the local slope parameter, defined as the ratio between the topographic slope and the depth-averaged isopycnal slope, in controlling the nonlinear eddy buoyancy fluxes. Both the GEOMETRIC framework and the CF scaling can reproduce the depth-averaged eddy buoyancy transfer across alongshore-uniform continental slopes, for suitably chosen constant prefactors. Generalization of these scalings across both continental slope and open ocean environments requires the introduction of prefactors that depend on the local slope parameter via empirically derived analytical functions. In contrast, the MLT-based scalings fail to quantify the eddy buoyancy transfer across alongshore-uniform continental slopes when constant prefactors are adopted, but can reproduce the cross-slope eddy flux when the prefactors are adapted via empirical functions of the local slope parameter. Application of these scalings in prognostic ocean simulations also depends on an accurate representation of standing eddies associated with the topographic corrugations of the continental slope. These findings offer a basis for extending existing approaches to parameterizing transient eddies, and call for future efforts to parameterize standing eddies in coarse-resolution ocean climate models.

Keywords:
Mesoscale eddies, continental slopes, eddy parameterization, eddy transfer coefficient, eddy-mean flow interactions.

1. Introduction

Continental slopes compromise a large fraction of the steepest areas of the sea floor (LaCasce, 2017), and connect the shallow continental shelves and the deep open ocean (Cacchione et al., 2002). The topographic potential vorticity (PV) gradient imposed by continental slopes is typically two to three orders of magnitude larger than the local planetary vorticity gradient (Cherian and Brink, 2018), favoring the orientation of large-scale flows along the slope (Brink, 2016) and inhibiting cross-slope transfer (*e.g.*, Olascoaga et al. 2006). Most along-slope flows, however, are also associated with sharp density fronts and horizontal velocity shears that may be subject to baroclinic and barotropic instabilities (LaCasce et al., 2019), from which mesoscale eddies can develop and mediate the cross-slope exchange (*e.g.*, Bower et al., 1985). Indeed, mesoscale eddies are increasingly documented to control the transport of heat, salt, and biogeochemical tracers between the coastal and the open oceans, and consequently modulate water mass formations and ocean general circulation (Spall, 2004; Pickart and Spall, 2007; Spall, 2010; Jungclaus and Mellor, 2000; Serra and Ambar, 2002; Dinniman et al., 2011; Nøst et al., 2011; Hattermann et al., 2014; Stewart and Thompson, 2012, 2015).

Increases in computing power have allowed global ocean models to be run with a horizontal grid spacing as fine as 0.1^o (*e.g.* Uchida et al. 2017), resolving mesoscale at low and mid-latitudes in the open ocean. However, even with such a fine resolution, mesoscale eddies cannot be resolved over continental slopes (Hallberg, 2013). The rapid decrease of the ocean depth leads to a decrease of the Rossby deformation radius and thus finer scales of unstable baroclinic modes compared to those in the open ocean. In addition, recent studies have revealed that baroclinic modes tend to be surface intensified over steep topography (LaCasce, 2017) and require high vertical resolution to simulate in ocean models cast in geopotential coordinates

(*e.g.* Stewart et al., 2017). Numerical experiments on freely evolving and wind-driven baroclinic turbulence over topography point towards a bottom-intensified eddy energy sink due to topographic rectification even in the absence of tides (Merryfield and Holloway 1999; Venaille 2012; Wang and Stewart 2018, WS18 hereafter), indicating that eddy effects at the surface substantially differ from those near the sloping bottom (*e.g.* LaCasce 1998; LaCasce and Brink 2000). This invites the question: to what extent do existing eddy parameterizations adopted by today's ocean climate models capture eddy behaviors over continental slopes?

The most widely used approach to parameterizing mesoscale eddies in coarse-resolution ocean climate models is a combination of the Gent and McWilliams (1990, GM hereafter) scheme, which works to flatten isopycnals and release potential energy, and the Redi (1982) scheme, which serves to flux tracers downgradient along isopycnals. This approach hinges upon the prescription of the GM and Redi eddy transfer coefficients, which measure the strengths of adiabatic buoyancy and isopycnal mixing by transient eddies, respectively, depending on the large-scale, explicitly resolved flow properties. In the quasi-geostrophic (QG) ocean interior, the GM transfer coefficent can be approximately related to the Redi transfer coefficient (Abernathey et al., 2013), therefore accurate construction of the former may shed light on the latter.

Various schemes have been proposed to construct the GM eddy transfer coefficient using properties of the resolved flow. For instance, the mixing length theory (MLT hereafter, Prandtl 1925) paradigm formulates the GM transfer coefficient as the product of an eddy length scale and a characteristic eddy velocity (or equivalently the product of an inverse eddy time scale and the squared eddy length scale), multiplied by a non-dimensional prefactor coefficient (*e.g.* Green 1970; Stone 1972; Visbeck et al. 1997; Eden and Greatbatch 2008; Cessi 2008; Jansen et al. 2015). Other formulations have been derived from mathematical constraints on the eddy stress tensor (*e.g.* Marshall et al. 2012; Bachman et al. 2017; Mak et al. 2017, 2018), from scalings diagnosed from numerical experiments (*e.g.* Bachman and Fox-Kemper 2013), and from kinematic consideration of fluid parcel motions (Fox-Kemper et al., 2008). Although these approaches have achieved increasing fidelity in their representation of eddy restratification and transport in the open ocean (Griffies, 2004), they are not necessarily transferable to continental slopes.

Previous studies of cross-slope eddy buoyancy transfer have relied principally on the modified QG Eady (1949) or Phillips (1954) models, which predict that the ratio between the bottom slope and the isopycnal slope, denoted by the slope parameter δ, determines the stability of along-slope flows (Blumsack and Gierasch, 1972; Mechoso, 1980; Spall, 2004; Isachsen, 2011; Pennel et al., 2012; Poulin et al., 2014; Hetland, 2017; LaCasce et al., 2019; Manucharyan and Isachsen, 2019). Specifically, for $\delta < 0$, corresponding to prograde (*i.e.* in the same direction as the topographic wave propagation) flows, both the wavelengths and the growth rates of unstable waves decrease as the magnitude of δ increases. By contrast, for $\delta > 0$, corresponding to retrograde (*i.e.* opposite to the direction of topographic wave propagation) flows, the linear growth rate instead increases, but then drops to zero for $\delta > 1$. The linear prediction has proved to be qualitatively useful in interpreting the nonlinear eddy buoyancy transfer in prograde fronts via primitive equation simulations and laboratory experiments (Spall, 2004; Isachsen, 2011; Pennel et al., 2012; Poulin et al., 2014; Ghaffari et al., 2018). This contrasts with retrograde flows, in which the nonlinear eddy mixing persists (WS18, Manucharyan and Isachsen 2019), and may even be enhanced, when δ exceeds 1 (*e.g.* Isachsen 2011; Stewart and Thompson 2013). A theoretical basis for interpreting the variation of nonlinear eddy buoyancy flux with the slope parameter in retrograde fronts remains elusive (Isachsen, 2011).

Most of the aforementioned studies have also chosen to neglect the influence of topographic canyons/ridges on eddy buoyancy transfer across continental slopes. However, this choice carries certain caveats, because topographic canyons/ridges were found to be ubiquitous along realistic continental margins (see Fig. 5 of Harris and Whiteway (2011) for a global distribution of submarine canyons). A number of studies have revealed that topographic canyons/ridges can substantially enhance the onshore intrusions of mass and physical/biogeochemical properties in retrograde slope fronts (*e.g.* Kämpf 2007; Allen and Hickey 2010), which are directly linked to the arrested topographically trapped waves over canyons/ridges (Zhang and Lentz, 2017, 2018).

A paradigm for constructing the GM-based eddy transfer coefficient that accounts for the effects of the bottom slope is yet to be developed. Such a paradigm should incorporate the aforementioned nonlinear eddy characteristics over continental slopes, particularly in retrograde fronts where linear predictions proved to be ineffective. This article serves as a first step to fill this crucial gap by constructing multiple slope-aware and numerically implementable scalings of the depth-averaged cross-slope eddy buoyancy mixing, focusing on the case of flows driven by retrograde wind forcing. In the limit of a flat ocean bed, most scalings reduce to the formulations that have been tested in previous studies. Consistent with the findings of Harris and Whiteway (2011), we also investigate to what extent topographic canyons/ridges may impact the proposed scalings for transient eddy buoyancy fluxes. The rest of this article is organized as follows. In Section 2, we describe the model configurations employed in this study, compare the key characteristics of wind-driven flows over an alongshore-uniform slope and over a corrugated slope, and highlight the quantitative influence of topographic corrugation on eddy buoyancy transfer. In Section 3, we propose the scalings for the depth-averaged eddy buoyancy mixing across alongshore-uniform continental slopes. In Section 4, we assess the transferability of these scalings to alongshore-corrugated slopes. Discussion and conclusion follow in Section 5.

2. Numerical simulations

In this section, we describe the model configuration of our simulations, illustrate the simulated flow characters, and quantify the cross-slope eddy buoyancy fluxes. All experiments use the MIT general circulation model (MITgcm hereafter, Marshall

Table 1: List of parameters used in the reference model run. Italics indicate parameters that are independently varied between model runs.

	Value	Description
L_x	800 km	Zonal domain size
L_y	500 km	*Meridional domain size*
H	4000 m	Maximum ocean depth
Z_s	2250 m	Slope mid-depth
H_s	3500 m	Shelf height
Y_s	200 km	Mean mid-slope offshore position
λ_t	$+\infty$ km	*Alongshore bathymetric wavelength*
Y_t	0 km	*Mid-slope position excursion*
W_s	50 km	*Slope half-width*
Y_w	200 km	Peak wind stress position
L_r	50 km	Width of northern relaxation
T_r	7 days	Northern relaxation timescale
τ_o	0.05N m^{-2}	*Wind stress maximum*
L_w	400 km	Meridional wind stress width
ρ_0	1000 kg m^{-3}	Reference density
α	$1 \times 10^{-4}\ ^oC^{-1}$	*Thermal expansion coefficient*
C_p	4000 J kg$^{-1}\ ^oC^{-1}$	Specific heat of seawater
g	9.81 m^2 s^{-1}	Gravitational constant
f_0	1×10^{-4}s^{-1}	Coriolis parameter
A_4^m	2.9×10^8m^{4}s^{-1}	Biharmonic viscosity
$\triangle x$	2 km	Horizontal grid spacing
$\triangle z$	10.5 m–103.8 m	Vertical level spacing
$\triangle t$	131 s	Time step size

et al. 1997), the quantitative performance of which in simulating continenal shelf/slope eddies has been evaluated in WS18 against an isopycnal-coordinate model and a terrain-following coordinate model.

2.1. Reference model configuration

The configuration of our reference simulation follows that of WS18, the most salient details of which are reiterated here, with reference physical parameters summarized in Table 1. We consider a zonal channel with a continental shelf of 500 m depth located at the southern boundary of the domain. The shelf is deeper than most realistic continental shelves (*e.g.* Cacchione et al. 2002) to ensure that the flow field over the shelf and slope is adequately resolved. The ocean depth is 4000 m at the northern boundary and shoals from the center of the domain toward the shelf across an idealized continental slope. Specifically, the bathymetry $z = h(x, y)$ is defined by

$$h(x,y) = -Z_s - \frac{1}{2}H_s \tanh\left[\frac{y - Y_s - Y_t \sin(2\pi x/\lambda_t)}{W_s}\right], \qquad (1)$$

where $x \in [-L_x/2,\ L_x/2]$ is the along-slope distance (longitude) from the domain center, $y \in [0,\ L_y]$ is the offshore distance (latitude), $Z_s = 2250$ m denotes the slope mid-depth, $H_s = 3500$ m represents the shelf height, and $W_s = 50$ km is the slope half-width. The latitude of the center of the continental slope varies longitudinally (see Fig. 1), with mean position $Y_s = 200$ km, wavelength λ_t, and onshore/offshore excursion amplitude Y_t. The channel spans 800 km and 500 km in the along-slope and cross-slope directions, respectively. Throughout this work, we will use "along-slope" and "longitudinal" or "zonal" interchangeably, and similarly for the "cross-slope" with "latitudinal" or "meridional". The channel is posed on an f-plane, with a Coriolis parameter $f_0 = 1 \times 10^{-4}$s^{-1}, as changes in depth dominate the background PV gradient, and so the slope can be thought of as being oriented in any direction relative to meridians.

We use a horizontal grid spacing of 2 km and 70 vertical levels, with vertical grid spacing increasing from 10 m at the surface to over 100 m at the ocean bed. Partial grid cells with a minimum non-dimensional fraction of 0.1 are used to improve representation of flows over the continental slope (Griffies et al., 2000). Simulations conducted at higher (1 km) horizontal grid resolution or based on 133 vertical levels yielded no qualitative differences from the results reported below.

The channel is forced at the surface by a steady alongshore wind stress with a cross-shore profile defined by

$$\tau_x = -\tau_o \cdot \sin^2(y/L_w), \qquad 0 < y < L_w. \qquad (2)$$

Here τ_o =0.05 N/m^2 denotes the maximum strength of wind, which coincides with the mean offshore slope position $Y_s = 200$ km, $L_w = 400$ km measures for the width of forcing in the offshore direction, and the negative sign on the right-hand side of (2) corresponds to retrograde (*i.e.* westward) wind stress. No surface buoyancy flux is prescribed. At the ocean bed, the channel is subject to a drag stress with quadratic coefficient $C_d = 2.5 \times 10^{-3}$, serving as a sink for energy and momentum imparted by the surface wind stress.

Periodic boundary conditions are used in the alongshore direction. No-normal-flow conditions are imposed at the shoreward and offshore edges of the domain. The potential temperature is restored to a reference exponential profile across a sponge layer of 50 km width at the northern boundary, with a maximum relaxation time scale of 7 days, to facilitate the evolution of ocean flow into a statistically steady state. This effectively fixes the first baroclinic Rossby deformation radius

$$L_d = \frac{\int_{-|h|}^{0} N_s\, dz}{\pi f_0}, \qquad (3)$$

at approximately 18 km in the deep open ocean, where N_s is the buoyancy frequency.

The surface K-Profile Parameterization (KPP) (Large et al., 1994) is used with its default setting for the reference simulation. Because almost no difference is yielded by replacing the KPP with a large diffusivity of 100 m^2/s for parameterizing convective instabilities, all subsequent experiments follow the latter option for computational efficiency. In addition, an explicit biharmonic viscosity is used for numerical stability.

2.2. Experiments

A suite of experiments are performed by varying the reference settings in §2.1. Specifically, we independently adjust the maximum strength of wind, the thermal expansion coefficient, and importantly, the slope geometry, for each simulation, which are summarized in Table 2. We vary these dimensional parameters in such a way as to cover a wide range of continental slope configurations, characterized by five non-dimensional numbers discussed below, and meanwhile avoid redundant runs.

Table 2: Simulation parameters varied between the model experiments. For parameter definitions, refer to Table 1.

Experiment	L_y(km)	W_s(km)	λ_t(km)	Y_t(km)	τ_0(N/m^2)	$\alpha(10^{-4}\ ^oC^{-1})$
SMOOTH_Reference	500	50	$+\infty$	0	0.05	1.0
SMOOTH_0.5τ_0	500	50	$+\infty$	0	0.025	1.0
SMOOTH_1.5τ_0	500	50	$+\infty$	0	0.075	1.0
SMOOTH_2.0τ_0	500	50	$+\infty$	0	0.10	1.0
SMOOTH_0.5W_s	500	25	$+\infty$	0	0.05	1.0
SMOOTH_0.66W_s	500	33	$+\infty$	0	0.05	1.0
SMOOTH_1.5W_s	500	75	$+\infty$	0	0.05	1.0
SMOOTH_2.0W_s	500	100	$+\infty$	0	0.05	1.0
SMOOTH_0.5α	500	50	$+\infty$	0	0.05	0.5
SMOOTH_2.0α	500	50	$+\infty$	0	0.05	2.0
CORRUG_200λ_t12.5Y_t	600	50	200.0	12.5	0.05	1.0
CORRUG_200λ_t25Y_t	600	50	200.0	25.0	0.05	1.0
CORRUG_200λ_t37.5Y_t	600	50	200.0	37.5	0.05	1.0
CORRUG_200λ_t50Y_t	600	50	200.0	50.0	0.05	1.0
CORRUG_266.7λ_t50Y_t	600	50	266.7	50.0	0.05	1.0
CORRUG_400λ_t50Y_t	600	50	400.0	50.0	0.05	1.0
CORRUG_800λ_t50Y_t	600	50	800.0	50.0	0.05	1.0

The wind stress magnitude is quantified by a Rossby number defined as

$$R_\tau = \frac{\tau_0}{\rho_0 f_0^2 L_w H}, \tag{4}$$

which is varied between 1.56×10^{-6} and 6.25×10^{-6}, corresponding to a wind-driven overturning with its strength ranging from 0.25 m^2/s to 1.00 m^2/s per unit channel width and thus resembling those across the margins of mid-latitude gyres (*e.g.* Colas et al. 2013) and high-latitude marginal seas (*e.g.* Manucharyan and Isachsen 2019). The stratification off the shelf/slope is quantified via the non-dimensionalized buoyancy frequency

$$N^* = \frac{\int_{-H}^{0} N_s|_{y=L_y} dz}{\pi f_0 H}, \tag{5}$$

where $N_s|_{y=L_y}$ denotes the vertical buoyancy frequency at the northern boundary. The first baroclinic Rossby deformation radius determined by (5) measures from 12 km through 25 km, mimicking the *near-slope* ocean condition at mid-/high-latitudes (see, *e.g.* Fig. 6 and Fig. 8 of Chelton et al. 1998). The slope steepness is measured by

$$s_t = \frac{H_s}{2W_s}, \tag{6}$$

which is varied between 1.75×10^{-2} and 7.00×10^{-2}, corresponding to a topographic slope angle ranging from 1^o to 4^o in the meridional direction, consistent with typical slope steepnesses in the ocean (*e.g.* Cacchione et al. 2002). The corrugation (or roughness) of the sloping ocean bed is quantified by the non-dimensional alongshore bathymetric wavelength

$$\lambda_0 = \frac{\lambda_t}{2(W_s + Y_t)}, \tag{7}$$

and the depth variation of the slope

$$\Upsilon = \frac{\max(H_m) - \min(H_m)}{H}, \tag{8}$$

where H_m is the height of ocean bed at the mean mid-slope position $y = Y_s$. Similar parameters to (4) and (8) are defined by Brink (2010) to study tidal rectification over continental shelves and slopes in a barotropic ocean.

The simulations in Table 2 are categorized into two groups, one based on zonally uniform channels (names beginning with "SMOOTH") and the other characterized by along-slope topographic variations (names beginning with "CORRUG") with finite positive values of Y_t and λ_t in (1). Preliminary experimentation reveals that flows in the CORRUG runs may be affected by the northern sponge layer if the offshore excursions of the continental slope are sufficiently large. We therefore expanded the channel width to 600 km, while retaining identical relaxation at the northern 50-km-wide boundary, in all CORRUG simulations. Further expansion of the channel width to 800 km yielded negligible differences to the CORRUG results. To facilitate comparison between simulations, we partition the corrugated-slope domains into southern, central, and northern slope regions delineated by the latitudes $y \in [Y_s - W_s - Y_t,\ Y_s - W_s)$, $y \in [Y_s - W_s,\ Y_s + W_s]$, and $y \in (Y_s + W_s,\ Y_s + W_s + Y_t]$, respectively. As such, the central slope region of a zonally uniform channel is also its entire slope region since $Y_t = 0$ (see Fig. 1(c)–(d)). The southern and northern slope regions accommodate, if any, onshore intrusion of canyons and offshore excursion of ridges, respectively.

All model runs integrate the three-dimensional, hydrostatic Boussinesq momentum equations coupled with a linearized equation of state depending on potential temperature only. Each simulation is spun up from a resting state at a coarse 4 km resolution for 35 years until a statistically steady state is reached, as determined from the time series of total kinetic energy. The solutions are then interpolated onto a finer 2 km grid and rerun for another 15 years to re-establish statistical equilibrium. Daily outputs taken from the final 5 years are analyzed.

2.3. Simulated flows

Fig. 1(a)–(b) illustrate snapshots of sea surface potential temperature (color contours) along with topographic geometries in the reference simulation SMOOTH_Reference and in a simulation with a slightly corrugated continental slope, CORRUG_200λ_t12.5Y_t (λ_t = 200 km, Y_t = 12.5 km), respectively.

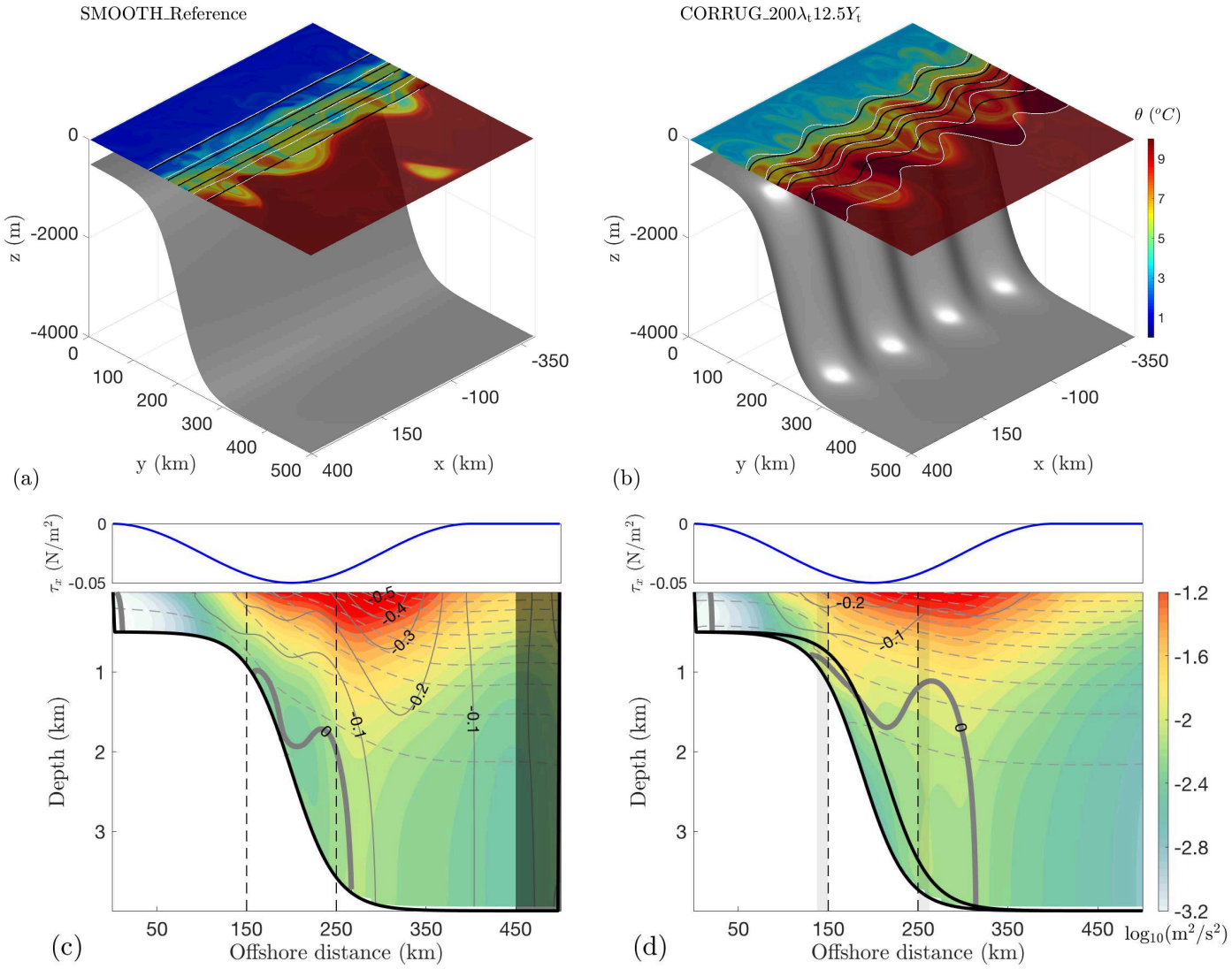

Figure 1: Schematic illustrations of the slope bathymetry used in (a) SMOOTH_Reference and (b) CORRUG_200λ_t12.5Y_t simulations, superposed by the snapshots of sea surface potential temperature (color), selected bathymetric contours (black), and selected quasi-streamlines of the time-mean sea surface horizontal velocity (white). Time-/zonal-mean eddy kinetic energy as a function of depth and offshore distance for the (c) SMOOTH_Reference and (d) CORRUG_200λ_t12.5Y_t runs, superposed by time-/zonal-mean isopycnals (dashed contours, interval: 1^oC) and alongshore velocity profiles (solid contours, interval: 0.1 m/s). The velocity contours $\overline{u}$ = 0 m/s are highlighted with bold lines. The upper panels of (c)–(d) illustrate the reference wind stress profile (blue line) used in this study, with negative signs corresponding to the retrograde direction. The northern sponge layer in the SMOOTH_Reference run is shadowed with dark gray in panel (c), and not shown for the CORRUG_200λ_t12.5Y_t run (in the latter the sponge layer lies between 550 and 600 km offshore). In panel (d), both the deepest and shallowest bathymetry contours at each latitude are plotted to illustrate the slight corrugation of the slope. The latitudes dividing the shelf/slope and slope/deep ocean are indicated by black dashed lines in panels (c)–(d). In panel (d), the northern and the southern slope regions are shadowed (see text in §2.2 for definitions of these regions).

Selected isobaths (black contours) and quasi-streamlines[1] of the time-mean horizontal velocity field $\overline{\mathbf{u}}_h$ at sea surface (white contours) are superposed on the potential temperature, where $\overline{\bullet}$ denotes a time average over the 5-year-long analysis period. Vigorous eddies are visible in both simulations. However, while the surface mean flow is almost exactly aligned with the isobaths in Fig. 1(a), standing meanders[2] with horizontal scales comparable to the zonal extent of the topographic variations arise and traverse the isobaths in Fig. 1(b). Numerous studies have shown that standing meanders in retrograde flows over a corrugated shelf/slope result from the arrested PV waves generated by topographic variations (Allen, 1975; Wang and Mooers, 1976; Csanady, 1978; Brink, 1986, 1991; Connolly et al., 2014; Zhang and Lentz, 2017, 2018), similar to those found in the Antarctic Circumpolar Current over a topographic ridge (Treguier and McWilliams, 1990; Stevens and Ivchenko, 1997; Abernathey and Cessi, 2014; Thompson and Naveira Garabato, 2014; Stewart and Hogg, 2017). Accompanying the standing meanders is the lower contrast of potential temperature between the shelf/slope and the open ocean, suggesting stronger restratification compared to the case shown in Fig. 1(a).

In Fig. 1(c)–(d), we quantify the time/zonal-averages of potential temperature $\left\langle \overline{\theta} \right\rangle$ and zonal velocity $\langle \overline{u} \rangle$, superposed on the logarithms of zonally averaged eddy kinetic energy (EKE) $\frac{1}{2}\left\langle \overline{u'^2} + \overline{v'^2} \right\rangle$ per unit mass, where $\langle \bullet \rangle = \frac{1}{L_x}\oint \bullet \, dx$ denotes the zonal-mean operator and the prime denotes the deviation of a quantity from its time-mean. EKE exhibits similar structures and magnitudes between the simulations. However, in the pres-

[1]The time-mean surface horizontal velocity fields in our simulations are not exactly divergence-free. The quasi-streamlines are selected contours of the quasi-streamfunction calculated as $\psi_{\text{surf}}(x,y) = \int_0^y \overline{u}(x,y)\Big|_{z=0} dy$.

[2]In this article we use the terms standing meanders, stationary meanders, and standing eddies interchangeably.

ence of standing meanders, the retrograde flow is weakened with its maximum strength shifted onshore, and the topographically induced prograde flow (see WS18 for the interpretation of prograde flow generation), where $u > 0$ m/s, occupies a larger area.

2.4. Cross-slope eddy buoyancy mixing

In this study, we specifically focus on developing scalings for transient eddy buoyancy fluxes across alongshore-uniform continental slopes, and then assessing the transferability of these scalings to corrugated continental slopes, which induce stronger restratification (Fig. 1(a)–(b)) and support weaker retrograde flows (Fig. 1(c)–(d)). For brevity, a detailed examination of the dynamics of mesoscale eddies over corrugated continental slopes is deferred to a future study. In the SMOOTH simulations, the cross-slope fluxes can be equivalently defined as those across the meridians or across the isobaths. Over a corrugated slope, however, these two types of fluxes differ. Meridional fluxes at a fixed latitude are determined by flows both over the ridges and within the canyons at the same latitude, and represent the deviations from the large-scale zonal-mean flow. This type of fluxes can be readily decomposed into a transient eddy part and a standing eddy part (*e.g.* Bischoff and Thompson 2014). However, the cross-isobath fluxes are confined above certain depths, and are directly shaped by the topographic PV gradient. This type of fluxes has been previously calculated to study fluid parcel exchanges between the shallow shelves and the open ocean (*e.g.* Brink 2010, 2011; Gan et al. 2009, 2013). Or, restated, meridional fluxes may include both cross-isobath and along-isobath components, whereas cross-isobath fluxes stress the motions traversing absolute depths. There is thus no reason to expect that a single scaling would apply to both types of eddy fluxes over a corrugated slope.

To illustrate the impact of standing meanders to the cross-slope buoyancy transfer by transient eddies, we first quantify the depth-averaged eddy buoyancy diffusivities in Fig. 2 as functions of latitude using the meridional transient eddy heat fluxes[3], defined by

$$\kappa_\theta = -\frac{F_\theta}{\left\langle \int_{-|h|}^{0} \overline{\theta}_y \, dz \right\rangle}, \tag{9a}$$

$$F_\theta = \left\langle \int_{-|h|}^{0} \overline{v'\theta'} \, dz \right\rangle. \tag{9b}$$

The definition (9a)–(9b) avoids ill-defined κ_θ in well-mixed regions by integrating the eddy buoyancy flux F_θ and mean buoyancy gradient separately (*e.g.* Jansen et al. 2015). Across the slope, κ_θ in the presence of canyons/ridges (red solid curve) ranges from -10 m^2/s at y = 150 km to 74 m^2/s at y = 250 km and is in general larger than that in the zonally uniform channel (for $y \geq 168$ km, blue curve), which ranges from 5 m^2/s to 26 m^2/s across the same latitudinal range, with its minimum reaching 3 m^2/s at $y \simeq 163$ km. The enhanced meridional buoyancy diffusivity produced by CORRUG_200λ_t12.5Y_t is consistent with the weakened meridional temperature gradient over the shelf/slope (Fig. 1(a)–(b)).

We then calculate the buoyancy diffusivity using the cross-isobath, rather than the meridional, heat fluxes:

$$\kappa_\theta^{iso}|_{h=h_0} = -\left. \frac{F_\theta^{iso}}{\oint \mathbf{n} \cdot \int_{-|h|}^{0} \nabla_H \overline{\theta} \, dz \, ds} \right|_{h=h_0}, \tag{10a}$$

$$F_\theta^{iso}|_{h=h_0} = \iint_{|h|\leq|h_0|} \left(\nabla \cdot \int_{-|h|}^{0} \overline{\mathbf{u}_h' \theta'} dz \right) dA. \tag{10b}$$

Here $h = h_0$ is a selected isobath, ∇_H is the horizontal gradient operator, $\mathbf{n} = -\nabla_H h / |\nabla_H h|$ is the offshore unit normal vector to the isobath, ds denotes the infinitesimal arclength along the selected isobath, $h = h_0$, and dA denotes an infinitesimal horizontal area. Although κ_θ^{iso} is defined as a function of $|h|$, it is mapped onto Fig. 2 (red dashed line) as a function of the mean offshore distance of each isobath. It should be noted that both (9b) and (10b) automatically eliminate the rotational component of transient eddy fluxes based on the two-dimensional divergence theorem (Marshall and Shutts, 1981; Fox-Kemper et al., 2003)[4]. In addition, calculation of $F_\theta^{iso}|_{h=h_0}$ via (10b) is far more efficient than using the isobath-normal components of the depth-integrated eddy fluxes, which have to be obtained by interpolating eddy fluxes from the regular model grids onto the lateral location of each isobath. The cross-isobath flux/gradient are exactly identical to the meridional flux/gradient for SMOOTH runs. The cross-isobath buoyancy diffusivity κ_θ^{iso} in CORRUG_200λ_t12.5Y_t is generally smaller in magnitude than the meridional diffusivity κ_θ in either of the simulations shown here over the continental slope.

3. Scaling cross-slope buoyancy mixing

Our findings in §2.3–§2.4 suggest that the cross-slope buoyancy transfer can be quantitatively modulated by standing eddies. For instance, standing eddies can drive stronger restratification (Fig. 1(a)–(b) and Fig. 2). Furthermore, topographically induced prograde flows, which were shown to be associated with upgradient buoyancy fluxes by transient eddies (see Fig. 10 of WS18), tend to be enhanced in the presence of standing eddies (Fig. 1(c)–(d)). These quantitative differences should be factored into the scaling/parameterization of cross-slope buoyancy transfer, which necessarily incorporate the effects of both transient and standing eddies. However, there is no basis yet for parameterizing standing eddy fluxes, which must be addressed in future work. The qualitative behavior of transient eddies, such as the surface intensification of EKE (Fig. 1(c)–(d)), nevertheless remain when topographic corrugation is introduced.

[3] As our simulations employ a linear equation of state depending on the potential temperature only, buoyancy flux is proportional to heat flux and we therefore use these two terms interchangeably in this article.

[4] It follows from two-dimensional divergence theorem that the total eddy flux across the boundary of a control area is equal to the integral of the divergence of eddy flux over this area. The rotational component of the eddy flux vanishes via the divergence operator upon area-integral. In a periodic channel model subject to no-normal-flow lateral boundary conditions, the divergent eddy flux can only traverse the open boundaries defined by isobaths.

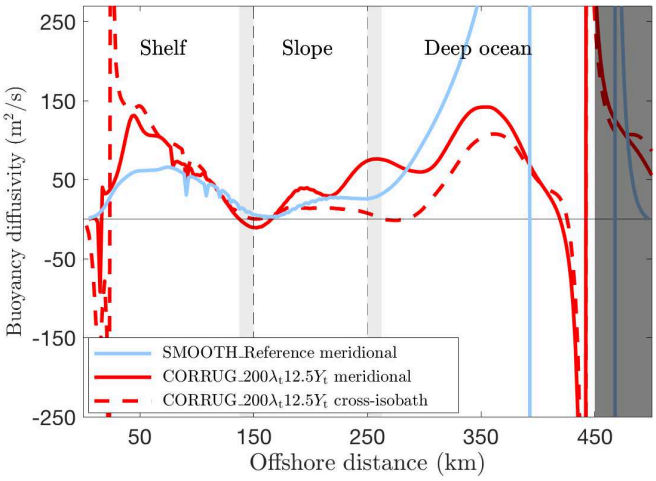

Figure 2: Depth-averaged eddy buoyancy diffusivities as functions of latitude. The northern sponge layer in SMOOTH_Reference is shadowed with dark gray. The northern/southern slope regions in CORRUG_200λ_t12.5Y_t are shadowed with light gray. Red solid (dashed) curve indicates the eddy buoyancy diffusivity in the meridional (cross-isobath) direction in the CORRUG_200λ_t12.5Y_t run. The blue curve indicates the eddy buoyancy diffusivity in the meridional direction, or equivalently in the cross-isobath direction, in the SMOOTH_Reference run.

This makes the SMOOTH simulations, which carry the advantage of isolating the transient eddy fluxes from the standing meanders, a natural starting point for our investigation.

In this article, we focus on the local (*i.e.* depth-averaged) cross-slope eddy buoyancy mixing, shown in Fig. 2, as a first step toward a more general parameterization. These diagnostics integrate the vertical structure of the eddy fluxes, which typically serve to restratify the ocean close to the surface, but destratify close to the bottom slope (WS18, see also Appendix A). However, even the depth-averaged eddy diffusivity may still turn negative over portions of the continental slope (see Fig. 2). We note that recently developed parameterizations of eddy transfer in the open ocean are formulated in terms of similar depth-averaged diffusivities (Jansen et al., 2015; Mak et al., 2017, 2018). In this section, we aim to derive scalings of eddy buoyancy mixing that transition smoothly from zonally uniform continental slopes to open ocean environments, and subsequently evaluate the transferability of these scalings to the corrugated continental slopes.

3.1. Parameter dependence of eddy buoyancy diffusivity

To assess the effect of mean (retrograde) flow properties on the cross-slope eddy mixing, one has several options to define a parameter space, within which three of the non-dimensional numbers are arguably the most crucial: the local slope parameter,

$$\delta_{\rm loc} = |\nabla_H h| \cdot \left(\int_{-|h|}^{0} N_s^2 \, dz \right) \Big/ \left(\mathbf{n} \cdot \int_{-|h|}^{0} \nabla_{\rm H} \bar{b} \, dz \right), \qquad (11)$$

the local Richardson number,

$$Ri_{\rm loc} = |h| f_0^2 \left(\int_{-|h|}^{0} N_s^2 \, dz \right) \Big/ \left(\mathbf{n} \cdot \int_{-|h|}^{0} \nabla_{\rm H} \bar{b} \, dz \right)^2, \qquad (12)$$

and the local slope Burger number,

$$Bu_{\rm loc} = \frac{|\nabla_{\rm h} h|}{f_0 |h|} \left(\int_{-|h|}^{0} N_s \, dz \right), \qquad (13)$$

where $\mathbf{n} = -\nabla_{\rm H} h / |\nabla_{\rm H} h|$ is the offshore isobath-normal unit vector. In the SMOOTH simulations, the lateral buoyancy gradient $\nabla_{\rm H} \bar{b}$ is almost exactly aligned with $\mathbf{n}$ (Fig. 1(a)), and we therefore have

$$\mathbf{n} \cdot \int_{-|h|}^{0} \nabla_{\rm H} \bar{b} \, dz \simeq \int_{-|h|}^{0} |\nabla_{\rm H} \bar{b}| \, dz \equiv \int_{-|h|}^{0} M^2 \, dz. \qquad (14)$$

Later in §4 we extend the definitions (11)–(12) to the CORRUG simulations, in which the mean flows are no longer parallel to the bathymetry (Fig. 1(b)).

In the modified QG Eady (1949) model, the slope parameter hinges upon the sign of the lateral PV gradient at the ocean bed, which determines the coupling of linear baroclinic modes at the bottom and at the surface (Vallis, 2006). The dynamic meaning of the slope parameter defined by (11) is much less obvious in more general cases where interior PV gradients become finite, but previous studies indicate that a quantitative relation between $\delta_{\rm loc}$ and cross-slope eddy diffusivity still exists (*e.g.* Isachsen 2011; Stewart and Thompson 2013). The Richardson number is an indicator of baroclinicity of the flow, and has been used in multiple studies to parameterize eddy buoyancy fluxes (*e.g.* Visbeck et al. 1997; Marshall et al. 2012; Bachman and Fox-Kemper 2013). Finally, recent study of Hetland (2017) suggests that the slope Burger number is critical in constraining the eddy growth in prograde fronts, while its role in retrograde fronts has yet to be determined. It should be noted that any two of these non-dimensional numbers can be used to approximate the third (Hetland, 2017),

$$\begin{aligned} Bu_{\rm loc} \cdot Ri_{\rm loc}^{1/2} &\sim \left[|\nabla_{\rm H} h| \frac{N_s}{f_0} \right] \left[\frac{N_s f_0}{M^2} \right] = \left[|\nabla_{\rm H} h| \right] \left[\frac{N_s^2}{M^2} \right] \\ &= \frac{\text{Bottom slope}}{\text{Isopycnal slope}} \sim \delta_{\rm loc}. \end{aligned} \qquad (15)$$

We also seek to understand the influences of three dimensional quantities on cross-slope eddy mixing: the (topographic) Rhines scale

$$L_{\rm Rh} = \sqrt{\frac{u_e}{\beta_t}}, \quad \beta_t = \frac{f_0}{|h|} |\nabla_H h|, \qquad (16)$$

the local EKE per horizontal area $\left\langle \frac{1}{|h|} \int_{-|h|}^{0} \text{EKE} \, dz \right\rangle$, or equivalently the eddy velocity scale adopted in (16),

$$u_e = \sqrt{\frac{2}{|h|} \int_{-|h|}^{0} \text{EKE} \, \text{dz}}, \qquad (17)$$

and the local eddy potential energy (EPE) per horizontal area (Aiki et al., 2016),

$$\frac{1}{|h|} \sum_{i=1}^{N_{\rm lay}-1} \text{EPE}_i = \frac{1}{|h|} \sum_{i=1}^{N_{\rm lay}-1} \frac{1}{2} \rho_0 g_i' \overline{\eta_{i+1/2}'^2}, \qquad (18)$$

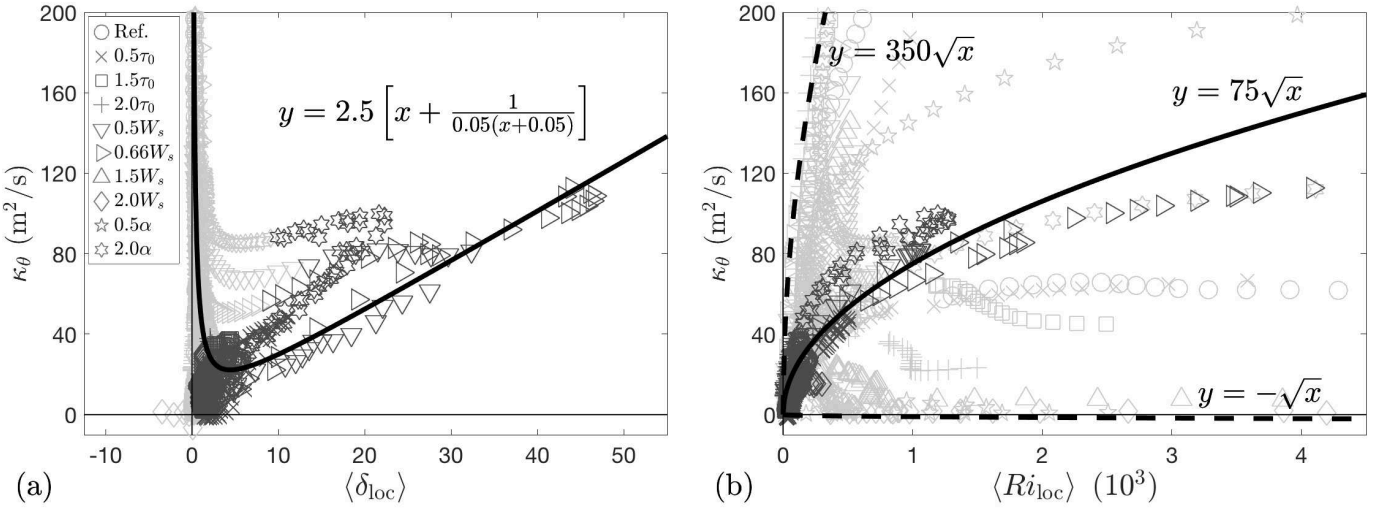

Figure 3: Scatter plots of the depth-averaged eddy buoyancy diffusivity against (a) the local slope parameter, and (b) the local Richardson number. All diagnostics are zonally averaged. Dark gray markers indicate diagnostics made over the slope, and light gray markers indicate diagnostics made from the peripheral regions of the slope (see Section 3.1 for definitions of different regions). Selected functional fits have been overlaid to quantify the relations between the physical parameters and the local eddy buoyancy diffusivity. The independent and dependent variables of the functional fits are represented by x and y, which should not be confused with the model domain coordinates.

where the subscript i denotes the counting of isopycnal layers from surface to bottom with its maximum denoted by $N_{\rm lay}$, $\eta_{i+1/2}$ is the isopycnal interface between layers i and $i+1$, and $g_i' = g(\rho_{i+1} - \rho_i)/\rho_0$ stands for the associated reduced gravity. The local EPE can be calculated either via the LAYERS package in MITgcm (*e.g.* Mak et al. 2018), or by converting the diagnostics on a geopotential coordinate system onto isopycnal coordinates following Young (2012); in this study, we follow the latter approach by selecting a total of $N_{\rm lay} = 71$ isopycnal layers, with buoyancy intervals selected based on the prescribed vertical discretization of the buoyancy field in the northern sponge layer. Previous studies have found these dimensional parameters to be salient in parameterizing eddy effects in the open ocean (*e.g.* Eden and Greatbatch 2008; Cessi 2008; Marshall et al. 2012; Jansen et al. 2015).

We diagnose the non-dimensional numbers (11)–(13), the dimensional quantities (16)–(18), and the cross-slope eddy buoyancy diffusivity κ_θ in portions of the model domain where the ocean depth lies between 510 m and 3990 m. For simulations with widened continental slopes, we further constrain the analysis to the region south of $y = 350$ km (*i.e.* at least 100 km away from the northern sponge layer) to avoid the influence of the lateral boundaries and the weak topographic PV gradient β_t in nearly flat regions. WS18 has shown (in their Fig. 3) that potential energy conversion from EKE may occur throughout the water column between $y = 350$ km and 450 km due to the buoyancy restoring at the northern boundary in the reference run.

These analysis regions, aggregated across all SMOOTH simulations, yield 1428 latitudinal bands from which to draw diagnostics of (11)–(13) and (16)–(18). We then zonally average and plot these parameters against κ_θ via gray markers in Fig. 3 and in Appendix B. Diagnostics made within the continental slope region $y \in [Y_s - W_s, Y_s + W_s]$, which are consistently between 938 m and 3568 m depths in our simulations, are highlighted using a darker gray tone. We stress that although these controlling parameters were coupled in several ways to parameterize baroclinic eddy fluxes in previous studies (*e.g.* Visbeck et al. 1997; Spall 2004; Jansen et al. 2015), each of them in isolation does not necessarily have a functional relationship with the eddy diffusivity.

Fig. 3(a) shows the relationship between the bottom slope steepness, relative to the isopycnal slope, and the cross-slope eddy buoyancy diffusivity. Consistent with previous studies based on primitive equation simulations (*e.g.* Isachsen 2011; Stewart and Thompson 2013), cross-slope eddy mixing is increasingly suppressed as δ deviates from 0 toward positive values. However, in contrast to the linear prediction (Blumsack and Gierasch, 1972; Mechoso, 1980), no stabilization of the flow is found for $\delta > 1$. In fact, the cross-slope eddy mixing appears to increase approximately linearly with δ for $\delta > 1$. The discrepancy between the linear prediction based on the modified Eady (1949) or Phillips (1951) model and the non-linear model results is mainly due to the lack of interior PV gradient and flow nonlinearity in the former (Trodahl and Isachsen, 2018; Ghaffari et al., 2018).

Many functional forms could be used to fit the relation between κ_θ and $\langle\delta_{\rm loc}\rangle$. Favoring simplicity, we use a sum of a linear function and a reciprocal function,

$$\kappa_\theta \sim \gamma\left[\langle\delta_{\rm loc}\rangle + \frac{1}{\varphi\langle\delta_{\rm loc}\rangle + \Gamma}\right], \tag{19}$$

as illustrated by Fig. 3(a). Here $\gamma = 2.5$ is the estimated slope of the linear functional part, $\varphi = 5 \times 10^{-2}$ is a constant that adjusts the decay rate of the reciprocal functional part, and $\Gamma \ll 1$ denotes a positive constant to accommodate the limit $\langle\delta_{\rm loc}\rangle \to 0$

(*i.e.* nearly flat ocean bed case). It should be noted that there is no theoretical basis for the functional fit (19). Following previous studies (*e.g.* Stewart and Thompson 2013), our approach is entirely empirical. The least-squares error produced by (19) decreases by a factor of 2 compared to a linear functional fit if diagnostics from both the continental slope and the open ocean regions are accounted for. When diagnostics from the continental shelf are also included, the relation (19) generates a slightly larger error than a linear fit, partly due to the emergence of negative eddy diffusivity and local slope parameter. This issue can be fixed by replacing the reciprocal function in (19) with an exponential decay. However, our key findings reported in later sections do not qualitatively depend on such modifications. Crucially, the mathematically simple form of (19) helps to simplify our analysis contrasted to most other nonlinear functions. The eddy diffusivity is then predicted to reach its minimum as $\langle \delta_{\rm loc} \rangle \simeq 4.42 \sim O(1)$. As the ocean bed becomes steeper, eddy mixing starts to be constrained by the linear functional part of (19). For $\langle \delta_{\rm loc} \rangle \to +\infty$ (*i.e.* zero projection of isopycnal slope in the cross-slope direction), this simple approximation becomes unbounded. We return to this point and discuss potential regularizations for this issue in §5.

Fig. 3(b) exhibits widespread scatter of the local Richardson number $\langle Ri_{\rm loc} \rangle$ against the eddy diffusivity κ_θ. Further examination suggests the relation

$$\kappa_\theta \sim \gamma \left\langle 10^{-3} Ri_{\rm loc} \right\rangle^{1/2}, \tag{20}$$

with γ varying from -1 to 350 depending on the simulations and geographic locations. Similar to (19), the relation (20) is empirical, selected from many possible nonlinear fits. The cases exhibiting weakly negative values of γ are those dominated by eddy destratification, which are relatively rare in the SMOOTH simulations (see §4). Over continental slopes, $\gamma \simeq 75$ yields a good fit for all simulations, with the least-squares error smaller than from an optimized linear fit by a factor of approximately 1.85. These results may seem counter-intuitive as higher Richardson number suggests weaker baroclinicity of the along-slope flow and thus lower available potential energy reservoir. In the classical Eady (1949) model, baroclinic mode growth rate is exactly proportional to $f_0/\sqrt{Ri}$ (*e.g.* Pedlosky 1987; Vallis 2006), suggesting an anti-correlation between κ_θ and $\langle Ri_{\rm loc} \rangle^{1/2}$ if the linear modes govern the eddy mixing. Existing eddy parameterizations also treat the Eady growth rate as a key parameter (*e.g.* Visbeck et al. 1997; Marshall et al. 2012).

The relationships between the eddy diffusivity and the other selected parameters, (13) and (16)–(18), are shown in Appendix B. Of the potential controlling parameters explored, only the local slope parameter $\delta_{\rm loc}$ (in isolation) exhibits a strong functional relation with the eddy diffusivity in both the continental slope and open ocean environments. Although the local Richardson number $Ri_{\rm loc}$ constrains eddy buoyancy fluxes across the continental slope, and has been incorporated in existing eddy parameterizations (*e.g.* Visbeck et al. 1997; Marshall et al. 2012; Bachman and Fox-Kemper 2013), the eddy buoyancy diffusivity cannot be scaled by $Ri_{\rm loc}$ alone in the open ocean environment. Other parameters (in isolation) may exhibit functional relationships with the eddy diffusivity in the open ocean, but not over the continental slope (see Appendix B). These findings suggests that existing eddy parameterizations may be adaptable to continental slopes via the introduction of a dependence on the local slope parameter, as shown in the following sections.

3.2. Scaling of eddy mixing via the GEOMETRIC framework

The observation that κ_θ tends to scale with $\langle Ri_{\rm loc} \rangle^{1/2}$ (Fig. 3(b)) motivates the application of a recently developed paradigm of eddy parameterization that combines the square root of the Richardson number with the *total* eddy energy, namely, the GEOMETRIC framework (Marshall et al., 2012; Bachman et al., 2017; Mak et al., 2017, 2018). Specifically, Marshall et al. (2012) defined

$$\kappa_{\rm Geom} = \gamma_{\rm Geom} \frac{N_s}{M^2} E = \gamma_{\rm Geom} \frac{\sqrt{Ri}}{f_0} E, \tag{21}$$

based on a geometric constraint on the Eliassen-Palm flux tensor in quasi-geostrophic flows. Here $\gamma_{\rm Geom}$ is a non-dimensional prefactor, whose magnitude is bounded by unity, and E denotes the sum of the EKE and the EPE per unit mass. In a coarse-resolution ocean model, if an additional prognostic equation for the subgrid eddy energy budget is implemented (*e.g.* Mak et al. 2018), the only free parameter in (21) is $\gamma_{\rm Geom}$, which contains the information about the partition between the EKE and EPE, and the anisotropy of the eddy buoyancy fluxes (Marshall et al., 2012).

It should be noted that the cross-slope eddy diffusivity can turn negative, even in a depth-averaged sense, over zonally uniform slopes (Fig. 3). This contradicts other eddy parameterizations that permit vertically local destratification of flows by baroclinic eddies, but ensure net potential energy destruction across a full water column (*e.g.* Ferrari et al. 2010). This further motivates the application of the GEOMETRIC framework over steep slopes: the coefficient $\gamma_{\rm Geom}$ may become predominantly negative across a water column if the relative orientation of the eddy buoyancy flux to the mean buoyancy gradient is sufficiently small (Marshall et al., 2012).

Fig. 4(a) demonstrates the performance of the local GEOMETRIC scaling,

$$\kappa_{\rm Geom} = \gamma \frac{\sqrt{Ri_{\rm loc}}}{f_0} E_{\rm loc}, \tag{22a}$$

$$E_{\rm loc} = \frac{1}{|h|} \left(\int_{-|h|}^{0} {\rm EKE}\, dz + \sum_{i=1}^{N_{\rm lay}-1} {\rm EPE}_i \right), \tag{22b}$$

in quantifying κ_θ over continental slopes. Here $\gamma = \gamma_{\rm Geom} = 1.08 \times 10^{-2}$ is a constant that optimizes the linear fit between the scaling (22a–b) and the diagnosed diffusivities, and $E_{\rm loc}$ denotes the depth-averaged total eddy energy per unit mass. A strong correlation ($r^2 = 0.87$) is found. The prefactor $\gamma \simeq 1.08 \times 10^{-2}$ is smaller than proposed by Mak et al. (2018) for open-ocean applications by a factor of almost 4, reflecting the much less efficient extraction of the mean-flow energy via

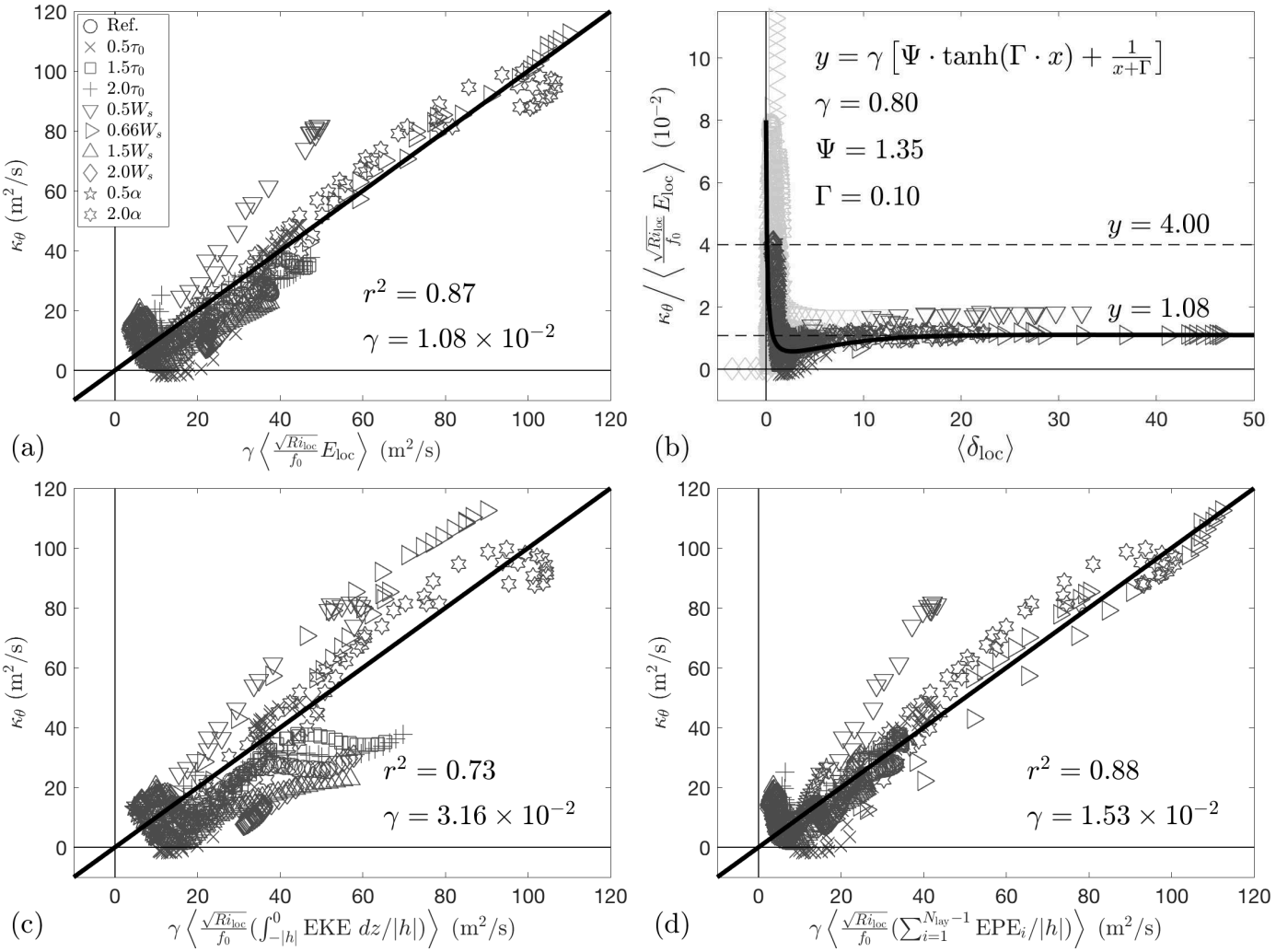

Figure 4: (a) Scatter plot of the depth-averaged eddy buoyancy diffusivity against the local GEOMETRIC scaling with a constant coefficient chosen to optimize the linear fit. (b) Illustration of the variation of the local GEOMETRIC prefactor as a function of the local slope parameter, which can be approximated by an analytical function. (c) Scatter plot of the depth-averaged eddy buoyancy diffusivity against a modified local GEOMETRIC scaling defined via the depth-averaged EKE, with a constant coefficient chosen to optimize the linear fit. (d) Same as in panel (c) but with the depth-averaged EKE replaced by the depth-averaged EPE. Dark gray markers indicate diagnostics made across the slope region. Light gray markers in panel (b) indicate diagnostics made from the open ocean and shelf regions (see text in §3.1 for definitions of these regions). All diagnostics have been zonally averaged. The correlation coefficients quoted in each panel are all statistically significant at the 1% level. The independent and dependent variables of the functional fits are represented by x and y in panel (b), which should not be confused with the model domain coordinates.

downgradient eddy buoyancy fluxes over steep slopes (Marshall et al., 2012; Bachman et al., 2017) and the bulk compensation between surface-intensified baroclinic instability and bottom-trapped eddy destratification (WS18).

The transition of the local GEOMETRIC prefactor

$$\gamma_{\rm Geom} = \kappa_\theta \Big/ \left\langle \frac{\sqrt{Ri_{\rm loc}}}{f_0} E_{\rm loc} \right\rangle \tag{23}$$

from the continental slopes toward the nearly flat regions can be quantified via the local slope parameter, and is illustrated in Fig. 4(b). Approaching the nearly flat regions, the prefactor ranges from 0 to over 0.1 with a median of approximately 0.04, consistent with the values adopted in idealized simulations of the Antarctic Circumpolar Current (Mak et al., 2017, 2018). Over continental slopes, $\gamma_{\rm Geom}$ tends to converge between 0.01 and 0.02. The weakest mixing is found for $\langle \delta_{\rm loc} \rangle$ between 0.5 and 4.0. A preliminary parameterization of (23) that captures this trend,

$$\gamma_{\rm Geom} = \gamma F_{\rm Geom}(\delta_{\rm loc}), \tag{24a}$$

$$F_{\rm Geom}(\delta_{\rm loc}) = \Psi \cdot \tanh(\Gamma \cdot \delta_{\rm loc}) + \frac{1}{\delta_{\rm loc} + \Gamma}, \tag{24b}$$

is presented in Fig. 4(b), where $\gamma \sim O(10^{-2})$ denotes a constant coefficient that sets the overall magnitude of the GEOMETRIC prefactor, and $F_{\rm Geom}$ is an empirical function that measures the variation of $\gamma_{\rm Geom}$ with $\delta_{\rm loc}$. Two parameters are defined in $F_{\rm Geom}$ and summarized in Table 3: $\Psi = 1.35$ captures the (re-scaled) GEOMETRIC prefactor over steep slopes, and $\Gamma = 0.1$ controls the asymptotic approach of $F_{\rm Geom}$ to Ψ for large $\delta_{\rm loc}$ and avoids $F_{\rm Geom}$ becoming ill-defined as $\delta_{\rm loc} \to 0$. Equation (24a) is then bounded by $\gamma/\Gamma \simeq 0.08$ (*i.e.* twice as large as the value used by Mak et al. 2018) as $\delta_{\rm loc} \to 0$, and converges to $\gamma\Psi \simeq 0.01$ as $\delta_{\rm loc} \to +\infty$. Substitution of this parameterization in place of the constant coefficient in (22) yields a closer agreement between $\kappa_{\rm Geom}$ and κ_θ, with their correlation raised to $r^2 = 0.92$. When the diagnostics from the open ocean

	GEOMETRIC	Cross-Front	Mixing Length theory
Slope-aware scalings	$\gamma F_{\text{Geom}}(\delta_{\text{loc}})\sqrt{Ri_{\text{loc}}}E_{\text{loc}}/f_0$	$\gamma F_{\text{CF}}(\delta_{\text{loc}})u_e\lvert h\rvert/S^{\theta}_{\text{loc}}$	$\gamma F_{\text{MLT}}(\delta_{\text{loc}})u_e L_{\text{Rh}}$
Empirical functions $F_{\text{Geom}}(\delta_{\text{loc}})$,			
$F_{\text{CF}}(\delta_{\text{loc}})$, and $F_{\text{MLT}}(\delta_{\text{loc}})$	$\Psi\cdot\tanh(\Gamma\cdot\delta_{\text{loc}})+\frac{1}{\delta_{\text{loc}}+\Gamma}$	$\Psi\cdot\tanh(\Gamma\cdot\delta_{\text{loc}})+\frac{1}{2\delta_{\text{loc}}+\Gamma}$	$\delta_{\text{loc}}+\frac{1}{\delta_{\text{loc}}+\Gamma}$
Overall magnitude of γ			
(cross-slope-averaged)	8.0×10^{-3}	8.0×10^{-4}	3.3×10^{-3}
Selected value of Ψ	1.35	0.50	N/A
Selected value of Γ	0.10	0.10	0.01

Table 3: List of the slope-aware scalings of cross-slope eddy diffusivity proposed in this study. The local slope parameter δ_{loc} is given by (11); the local Richardson number Ri_{loc} is given by (12); the eddy velocity scale u_e is given by (17); the local eddy energy E_{loc} is given by (22b); S^{θ}_{loc} denotes the local isopycnal slope projected onto the cross-isobath direction and is approximated by (28b) over alongshore uniform slopes; the empirical functions F_{Geom}, F_{CF}, and F_{MLT} are given by (24b), (29b), and (46b), respectively.

(both the open ocean and the continental shelf) are included, the diagnosis-scaling correlation is $r^2 = 0.61$ ($r^2 = 0.45$, not plotted) with a constant prefactor, but reaches $r^2 = 0.90$ ($r^2 = 0.76$) with the parameterization (24), as illustrated in Fig. 5(a).

Following Bachman et al. (2017), we proceed to investigate whether the predictive power of the GEOMETRIC scaling subject to a constant prefactor is constrained by differing eddy energy types used in (22b). To this end, we recalculate κ_{Geom} with the total eddy energy E_{loc} in (22a) replaced by either the local EKE or the local EPE. Fig. 4(c)–(d) indicates that although both energy types serve to establish positive correlations between the GEOMETRIC scaling and the diagnosed eddy diffusivity, the local EPE appears to play a more important role over steep slopes. This is in contrast with the finding of Bachman et al. (2017) that the predictive skill of the GEOMETRIC formula is independent of the eddy energy type adopted over a flat-bottomed ocean.

3.3. The Cross-Front scaling of eddy buoyancy transfer

We next formulate an alternative scaling for the cross-slope eddy buoyancy transfer. Conventional dimensional arguments suggest that the eddy diffusivity can be defined as the product of a squared length scale and a inverse time scale (*c.f.* §1). Here we use the topographic Rhines scale and the constant Coriolis frequency to construct our scaling. We stress that these choices are made based entirely on a variety of trials (not shown), rather than upon any theoretical basis. Because neither quantity in isolation has a functional relationship with the eddy diffusivity over the continental slope (Appendix B), we further affix a local slope parameter to capture the variation of the eddy diffusivity over steep slopes shown in Fig. 3(a), and define

$$\kappa_{\text{CF}} = \gamma_{\text{CF}}\delta_{\text{loc}}L^2_{\text{Rh}}f_0. \tag{25}$$

Here γ_{CF} is a non-dimensional coefficient, and the subscript "CF" stands for "Cross-Front". This name was motivated by an alternative writing of (25),

$$\begin{aligned}\kappa_{\text{CF}} &\sim \delta_{\text{loc}}\cdot L^2_{\text{Rh}}\cdot f_0\\ &\sim \frac{|\nabla_H h|\cdot N_s^2}{M^2}\cdot\frac{u_e}{\beta_t}\cdot f_0\\ &= \frac{f_0|\nabla_H h|}{|h|}\cdot|h|\cdot\frac{N_s^2}{M^2}\cdot\frac{u_e}{\beta_t}\\ &= \beta_t\cdot|h|\cdot\frac{N_s^2}{M^2}\cdot\frac{u_e}{\beta_t}\\ &= u_e\cdot\left(\frac{N_s^2}{M^2}|h|\right),\end{aligned} \tag{26}$$

which is a MLT-like scaling with the characteristic eddy velocity defined in (17), and the eddy length scale $\frac{N_s^2}{M^2}|h|$ measuring the horizontal distance required for the tilted isopycnals to span the entire ocean depth. The rearrangement (26) suggests that κ_{CF} does not explicitly depend on the topographic steepness, but rather on the isopycnal slope, if γ_{CF} is defined as a constant.

The local CF scaling, following (26),

$$\kappa_{\text{CF}} = \gamma\, u_e|h|\left(\int_{-|h|}^{0} N_s^2\, dz\right)\Big/\left(\int_{-|h|}^{0} M^2\, dz\right), \tag{27}$$

exhibits a strong correlation ($r^2 = 0.83$) with the diagnosed cross-slope eddy diffusivity (Fig. 6(a)), where $\gamma = \gamma_{\text{CF}} = 4\times10^{-4}$ has been chosen to optimize the linear fit. The correlation reduces to $r^2 = 0.70$ if the diagnostics from the open ocean are included, and to $r^2 = 0.57$ if both the continental shelf and open ocean portions are accounted for (not shown), which indicates that a constant prefactor is appropriate over steep slopes but unable to make the scaling transition smoothly from slopes toward the more flat regions.

The transition of the local CF prefactor,

$$\gamma_{\text{CF}} = \kappa_\theta\Big/\left\langle u_e\frac{|h|}{S^{\theta}_{\text{loc}}}\right\rangle, \tag{28a}$$

$$S^{\theta}_{\text{loc}} = \left(\int_{-|h|}^{0} M^2\, dz\right)\Big/\left(\int_{-|h|}^{0} N_s^2\, dz\right), \tag{28b}$$

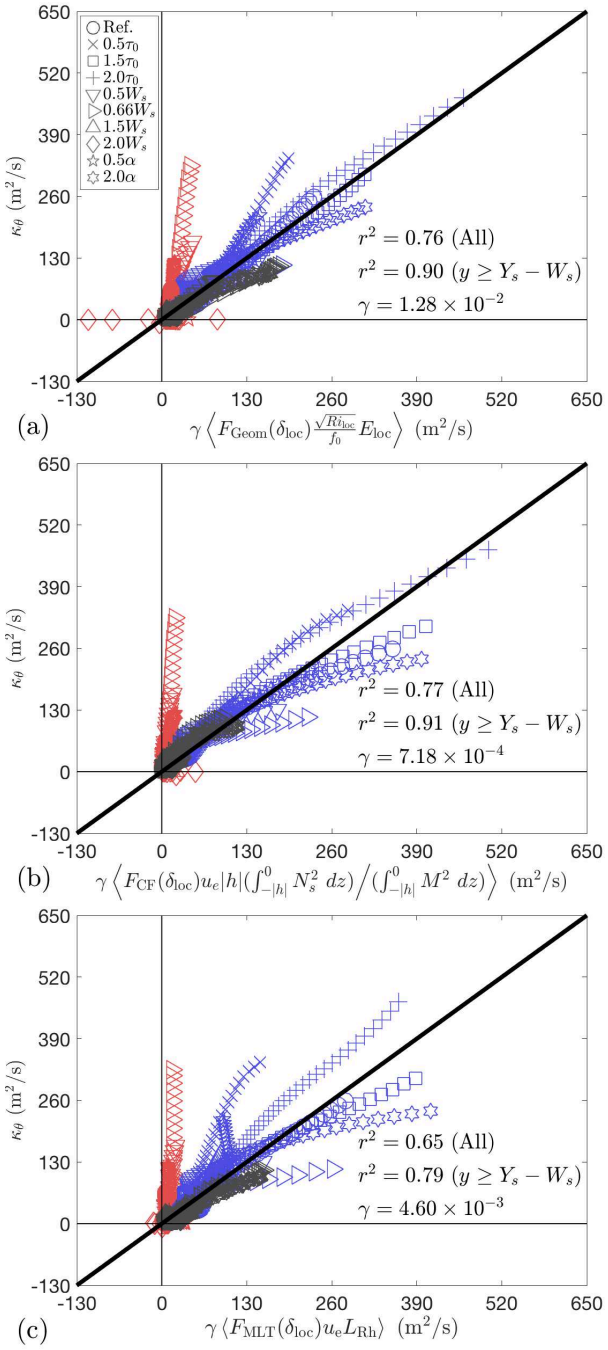

Figure 5: Scatter plots of depth-averaged eddy diffusivity against the slope-aware forms of (a) the local GEOMETRIC scaling, (b) the local CF scaling, and (c) the local MLT-based scaling, with constants γ selected to optimize the linear fit in each panel. Red markers indicate diagnostics made to the south of slope regions with shallowest depth bounded by 510 m. Blue markers indicate diagnostics collected to the north of slope regions with deepest depth bounded by 3990 m and northernmost location bounded by y = 350 km. Gray markers indicate diagnostics made across the slope region. The functions $F_{\rm Geom}$, $F_{\rm CF}$, and $F_{\rm MLT}$ are given by (24b), (29b), and (46b), respectively, and summarized in Table 3. The correlation coefficients quoted in each panel are all statistically significant at the 1% level.

from the continental slope to the nearly flat regions can be parameterized in terms of $\langle \delta_{\rm loc} \rangle$ following the approach described in §3.2, as shown in Fig. 6(b). We propose a functional relation between the CF scaling prefactor and the local slope parameter that is similar to (24),

$$\gamma_{\rm CF} = \gamma F_{\rm CF}(\delta_{\rm loc}), \tag{29a}$$

$$F_{\rm CF}(\delta_{\rm loc}) = \Psi \cdot \tanh(\Gamma \cdot \delta_{\rm loc}) + \frac{1}{2\delta_{\rm loc} + \Gamma}, \tag{29b}$$

where $\gamma \sim O(10^{-3})$ is a constant that sets the overall magnitude of $\gamma_{\rm CF}$. As in (24b), the parameters in (29b), $\Psi = 0.5$ and $\Gamma = 0.1$, are selected to approximate the variation of the empirical function $F_{\rm CF}$ with $\delta_{\rm loc}$ (see Table 3). Then it follows that that $\gamma_{\rm CF}$ is bounded by $\gamma/\Gamma \simeq 8 \times 10^{-3}$ in the flat bottom limit and converges to $\gamma\Psi \simeq 4 \times 10^{-4}$ over steep slopes. Replacement of the constant coefficient in (27) with the parameterization (29) yields a diagnosis-scaling correlation of $r^2 = 0.86$ over steep slopes, and of $r^2 = 0.91$ ($r^2 = 0.77$) if one includes the diagnostics from the open ocean region (both the open ocean and the shelf regions), as shown in Fig. 5(b).

Next we assess which of the variables that constitute the eddy length scale are most crucial in predicting the cross-slope eddy diffusivity when $\gamma_{\rm CF}$ is fixed as a constant. In Fig. 6(c) we plot a simplified form of the CF scaling,

$$\kappa_{\rm CF} = \gamma u_e Z_s \left(\int_{-|h|}^0 N_s^2\, dz \right) \Big/ \left(\int_{-|h|}^0 M^2\, dz \right), \tag{30}$$

with which we maintain the spatially varying isopycnal slope but replace the ocean depth $|h|$ in (27) with the slope mid-depth Z_s (Table 1). Interestingly, the diagnosis-scaling correlation gets even stronger ($r^2 = 0.89$) compared to the case with the original local CF form (27). Further replacement of the local vertical stratification $\int_{-|h|}^0 N_s^2\, dz \big/ |h|$ with the cross-slope-averaged vertical stratification leads to

$$\kappa_{\rm CF} = \gamma u_e Z_s N_0^2 \Big/ \left(\frac{1}{|h|} \int_{-|h|}^0 M^2\, dz \right), \tag{31a}$$

$$N_0^2 = \left(\iint_{\rm slope} \frac{1}{|h|} \int_{-|h|}^0 N_s^2\, dz\, dA \right) \Big/ \left(\iint_{\rm slope} dA \right), \tag{31b}$$

where the subscript "slope" denotes the region over which the integral is performed. The modification (31) slightly changes the scatter pattern between the scaling and the diagnosed diffusivity, but not the predictive skill of the CF scaling (Fig. 6(d)). Equations (31a)–(31b) also indicate that the cross-slope eddy buoyancy fluxes, $F_\theta \simeq \kappa_{\rm CF} \left(\frac{1}{|h|} \int_{-|h|}^0 M^2\, dz \right)$, scale only with the characteristic eddy velocity u_e, reminiscent of the empirical findings by Stewart and Thompson (2016) that the eddy thickness fluxes across the Antarctica continental margin scale with u_e alone (see their Equation 25). If the isopycnal slope quantity in (27) is substituted by its cross-slope-average, the correlation between κ_θ and $\kappa_{\rm CF}$ is diminished ($r^2 = 0.69$, not shown). Maintaining the spatially varying ocean depth and local vertical stratification while replacing the spatially varying horizontal stratification with its cross-slope-average produces a even lower correlation between the scaling and the diagnosed eddy diffusivity

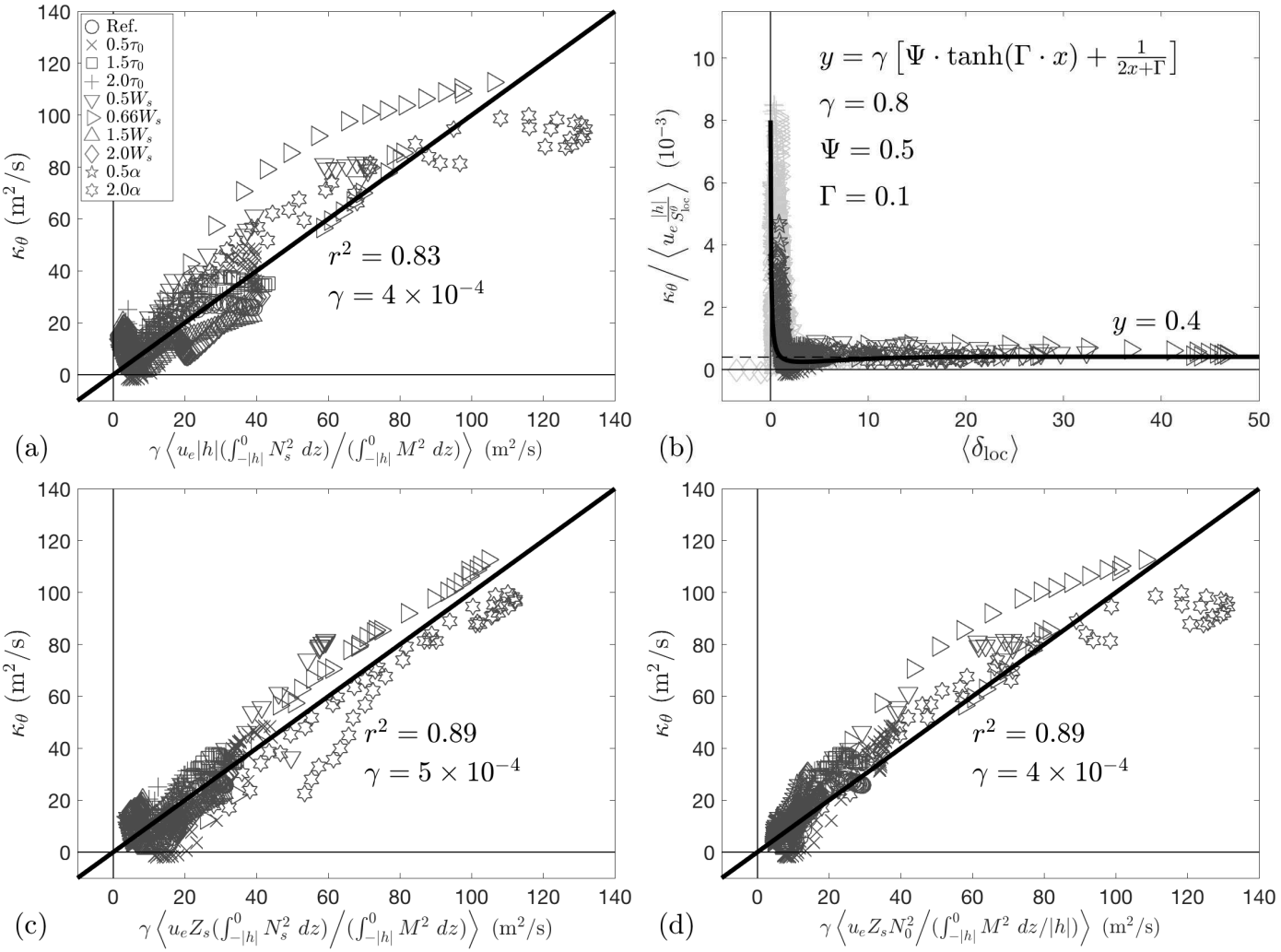

Figure 6: (a) Scatter plot of the depth-averaged eddy buoyancy diffusivity against the local CF scaling subject to a constant coefficient chosen to optimize the linear fit. (b) Illustration of the variation of the local CF prefactor as a function of the local slope parameter, which can be approximated by an analytical function. (c) Scatter plot of the depth-averaged eddy buoyancy diffusivity against the modified local CF scaling defined by maintaining the spatially varying isopycnal slope but replacing the ocean depth with the slope mid-depth. A constant coefficient is chosen to optimize the linear fit. (d) Scatter plot of the depth-averaged eddy buoyancy diffusivity against the modified local CF scaling defined by maintaining the spatially varying horizontal stratification, but replacing the ocean depth and the spatially varying vertical stratification with the slope mid-depth and the cross-slope-averaged vertical stratification, respectively. A constant coefficient is chosen to optimize the linear fit. Dark gray markers indicate diagnostics made across the slope region. Light gray markers in panel (b) indicate diagnostics made from the open ocean and shelf regions (see text in §3.1 for definitions of these regions). All diagnostics have been zonally averaged. The correlation coefficients quoted in each panel are all statistically significant at the 1% level. The independent and dependent variables of the functional fits are represented by x and y in panel (b), which should not be confused with the model domain coordinates.

($r^2 = 0.41$, not shown). Implementation of the CF formula over continental slopes for parameterization purposes should therefore preserve the spatial variation of the local isopycnal slope, or at least the horizontal stratification.

We note that (26) resembles the eddy buoyancy transfer coefficient proposed by Bachman and Fox-Kemper (2013),

$$\kappa_{\rm B13} = \gamma Ri^{-0.31} u_e \left(\frac{N_s^2}{M^2} |h| \right), \tag{32}$$

which is diagnosed from a set of Eady-like spin-down simulations (see also Bachman et al. 2017). Equation (32) differs from (26) by a factor of $Ri^{-0.31}$. Over the continental slope, the local Richardson number varies between $O(10) - O(10^3)$ (Fig. 3(b)), leading to the decrease of the predicted eddy diffusivity via $\kappa_{\rm B13}$ by a factor of 2-10 compared to $\kappa_{\rm CF}$. In Fig. 7(a) we plot the local form of

$$\kappa_{\rm B13} = \gamma Ri_{\rm loc}^{-0.31} u_e |h| \left(\int_{-|h|}^0 N_s^2\ dz \right) \Big/ \left(\int_{-|h|}^0 M^2\ dz \right) \tag{33}$$

against κ_θ with $\gamma = 2.5 \times 10^{-3}$ chosen to minimize the linear mismatch. The correlation ($r^2 = 0.59$) between the two quantities is much lower than the case shown in Fig. 6(a).

By replacing the eddy velocity scale u_e in (26) with the mean thermal wind velocity, one obtains the eddy transfer coefficient formulated by Fox-Kemper et al. (2008)

$$\kappa_{\rm FK08} = \gamma \frac{N_s^2 h^2}{f_0}, \tag{34}$$

which has been implemented to parameterize submesoscale eddy restratificaiton in the mixed layer in global ocean climate models (Fox-Kemper et al., 2011). As pointed out by Bachman et al. (2017), $\kappa_{\rm FK08}$ does not depend on the eddy energy budget

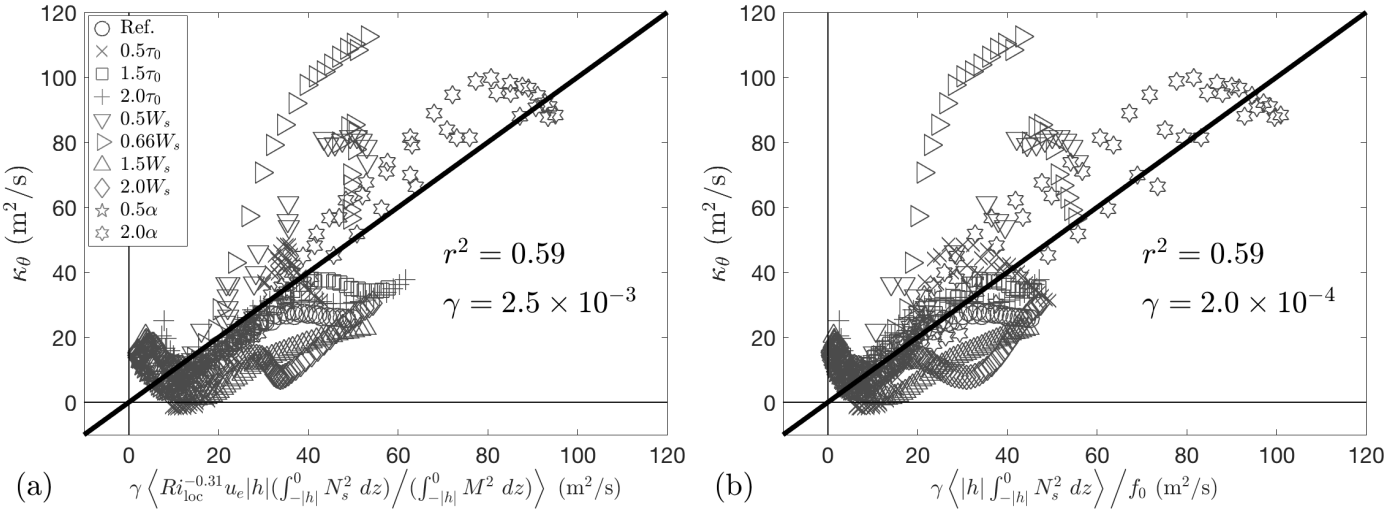

Figure 7: Scatter plots of the depth-averaged eddy buoyancy diffusivity against the local forms of the (a) Bachman and Fox-Kemper (2013) scaling and the (b) Fox-Kemper et al. (2008) scaling. Constant coefficients are selected to optimize the linear fits. Diagnostics are made across the continental slope region and zonally averaged. The correlation coefficients quoted in each panel are all statistically significant at the 1% level.

due to its differing definition of the characteristic velocity scale. In Fig. 7(b) we compare the local form,

$$\kappa_{\rm FK08} = \gamma |h| \left(\int_{-|h|}^{0} N_s^2 \, dz \right) \Big/ f_0, \tag{35}$$

with κ_θ, where $\gamma = 2 \times 10^{-4}$ optimizes the linear fit. An almost identical correlation ($r^2 = 0.59$) compared to the case shown in Fig. 7(a) is reached between κ_θ and $\kappa_{\rm FK08}$. While the weakened correlation between $\kappa_{\rm B13}$ and diagnostics sources from the Richardson number-dependent multiplier in (33), it is mainly the omission of the isopycnal slope quantity (*i.e.* M^2/N^2) that lowers the predictive skill of (35).

3.4. Slope-dependent mixing length theory

Although the original form of the CF scaling (25) incorporates the local slope parameter $\delta_{\rm loc}$, further transformation (26) frames it as a MLT-based scaling that is relatively insensitive to topographic steepness over continental slopes (see also Fig. 6(b)). It is then natural to ask whether other MLT-based eddy parameterizations, most of which do not explicitly incorporate topographic effects, apply to continental slopes. This question is also practical in that modern ocean general circulation models, such as the latest version of the Modular Ocean Model (MOM6), have a set of MLT-based eddy parameterizations implemented. Most of these parameterizations depend on a variety of optional length scales plus a prognostic subgrid EKE budget. To apply these parameterizations over continental slopes, one has to first select the most appropriate eddy length scale.

3.4.1. Previous mixing length theory-based scalings

Various studies have proposed that the eddy buoyancy transfer coefficient can be parameterized as

$$\kappa_{\rm MLT} \sim u_e l_e, \tag{36}$$

where u_e is drawn from the local EKE budget following (17) and l_e denotes an eddy length scale to be determined (*e.g.* Eden and Greatbatch 2008; Cessi 2008; Jansen et al. 2015). Recently, Jansen et al. (2015) has demonstrated that assigning the Rhines scale (defined via planetary vorticity gradient) as the eddy length scale such that

$$\kappa_{\rm MLT} \sim u_e L_{\rm Rh}, \tag{37}$$

broadly quantifies the eddy buoyancy mixing over a flat-bottomed ocean via a suite of idealized simulations (see their Fig. 6).

The eddy length scale has previously been defined as the "width of the baroclinic zone", across which baroclinic eddies were mostly generated (*e.g.* Visbeck et al. 1997; Bachman and Fox-Kemper 2013; Jansen et al. 2015). In the context of continental slope, one choice for the width of the baroclinic zone is the width of the slope (see Table 1), *i.e.*,

$$\kappa_{\rm MLT} \sim u_e W_s. \tag{38}$$

This formulation has been reported to accurately quantify the cross-slope eddy thickness flux in the Antarctic Slope Front (Stewart and Thompson, 2016).

Eden and Greatbatch (2008) have advocated to prescribe the eddy length scale not only by the Rhines scale, but also by the first Rossby radius of deformation such that

$$\kappa_{\rm MLT} \sim u_e \cdot \min(L_d,\, L_{\rm Rh}). \tag{39}$$

This approach was motivated by the observation that eddy mixing is more isotropic (anisotropic) and limited by the deformation radius (Rhines scale) at mid- (low) latitude (Eden, 2007). Others have chose to only use the deformation radius when testing eddy parameterizations (*e.g.* Cessi 2008).

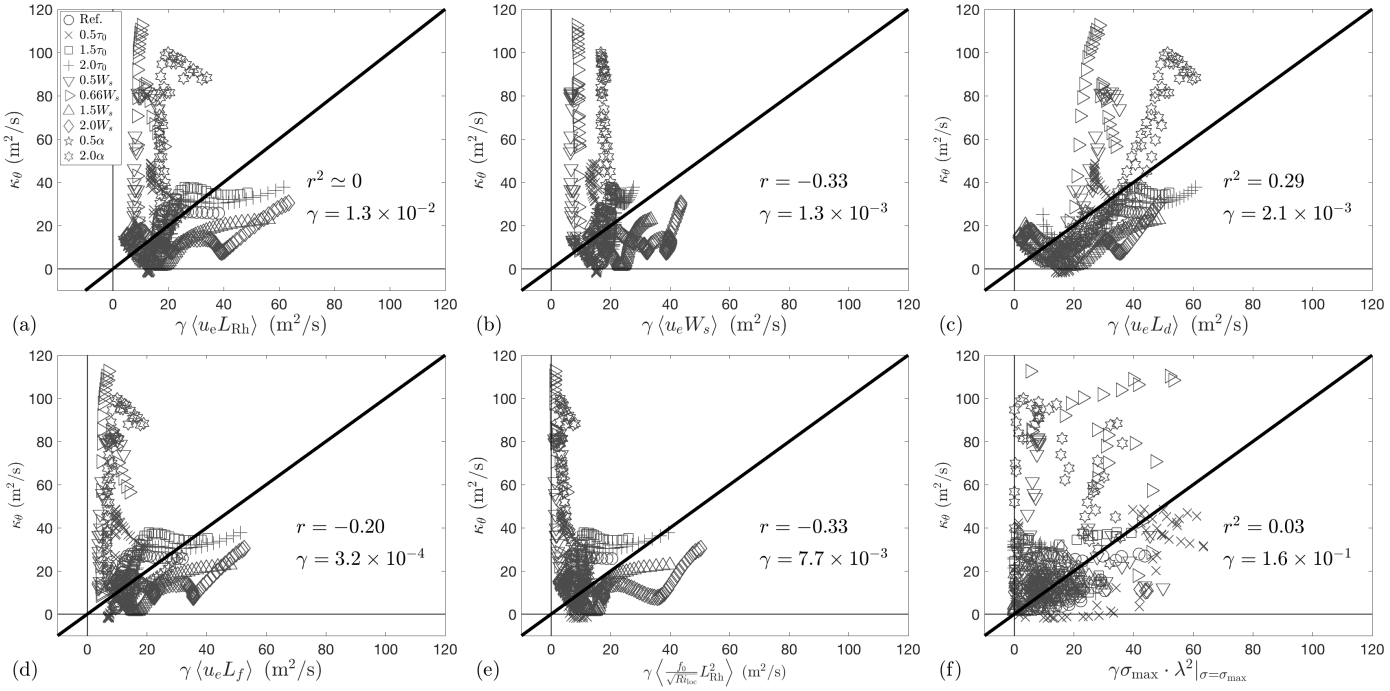

Figure 8: Scatter plots of the depth-averaged buoyancy diffusivity against MLT-based scalings constructed using (a) the product of the eddy velocity scale and the topographic Rhines scale, (b) the product of the eddy velocity scale and the slope half-width, (c) the product of the eddy velocity scale and the first Rossby radius of deformation, (d) the product of the eddy velocity scale and the frictional scale, (e) the Visbeck et al. (1997) variant, and (f) the Stone (1972) variant. All scalings are subject to constant coefficients chosen to optimize the linear fits. Diagnostics are made across the continental slope region and zonally averaged. Positive correlation coefficients have been squared and negative ones are shown directly. The p-value corresponding to the correlation coefficient quoted in panel (a) is 0.86. The correlation coefficients quoted in panels (b)–(f) are all statistically significant at the 1% level.

Eddy growth over a flat-bottomed ocean subject to quadratic bottom drag and vanishing PV gradient can also be limited by a frictional scale L_f (*e.g.* Jansen et al. 2015), leading to

$$\kappa_{\rm MLT} \sim u_e L_f, \quad L_f = \frac{h_e}{C_d}, \tag{40}$$

where h_e denotes the vertical scale of near-bottom flow. Over topography, h_e can be identified with the Prandlt $e-$folding scale (*e.g.* Rhines 1970; Treguier and McWilliams 1990; Merryfield and Holloway 1999; Brink 2016, see also Appendix A), and is naturally bounded by the ocean depth $|h|$, *i.e.*,

$$h_e \equiv \min\left[\frac{L_J f_0 |h|}{\int_{-|h|}^{0} N_s\, dz},\ |h|\right], \tag{41}$$

where $L_J \equiv L_{\rm Rh}$ stands for the width of near-bottom jets and has been defined as the topographic Rhines scale, consistent with previous studies (*e.g.* Maltrud and Vallis 1991, 1992; Thompson 2010; WS18). Equations (40)–(41) suggests that the jet width, which may represent the scale at which nonlinear eddies equilibrate, differs from the frictional scale by a factor of $C_d N_s/f_0$, which is far less than unity across the regions of our interest with its maximum below 0.08. We thereby speculate that the eddy growth are much less constrained by the frictional scale than by the topographic Rhines scale over continental slopes.

Fig. 8(a)–(d) compares κ_θ with the eddy transfer coefficient (36) via different choices for the eddy length scale. The correlations are invariably weak or even negative, which may have been anticipated as no quantitative trend is revealed between the diagnosed eddy diffusivity and the local topographic Rhines scale or the local EKE (see Appendix B).

It should be noted that the actual application of the scaling (36) as eddy parameterizations also requires the knowledge of the subgrid EKE, which is not always available in coarse-resolution ocean models. We therefore assess two additional scalings that are independent of the local EKE: one developed by Visbeck et al. (1997),

$$\kappa_{\rm V97} = \gamma \frac{f_0}{\sqrt{Ri}} l_e^2 = \gamma\, \sigma_{\rm E} l_e^2, \tag{42}$$

and the other by Stone (1972),

$$\kappa_{\rm S72} = \gamma \sigma_{\rm max} \cdot \lambda^2|_{\sigma=\sigma_{\rm max}}. \tag{43}$$

Here γ denotes the constant coefficient to be determined for each case, $\sigma_{\rm max}$ is the maximum growth rate of linear baroclinic waves, and $\lambda|_{\sigma=\sigma_{\rm max}}$ is the corresponding wavelength. Equation (42) defines the eddy velocity scale as the product of the eddy length scale l_e and the Eady growth rate $\sigma_{\rm E} \sim f_0/\sqrt{Ri}$, whereas (43) uses the product of the wavelength and growth rate of the most unstable baroclinic linear mode. Visbeck et al. (1997) assigned the width of baroclinic zone as the eddy length scale

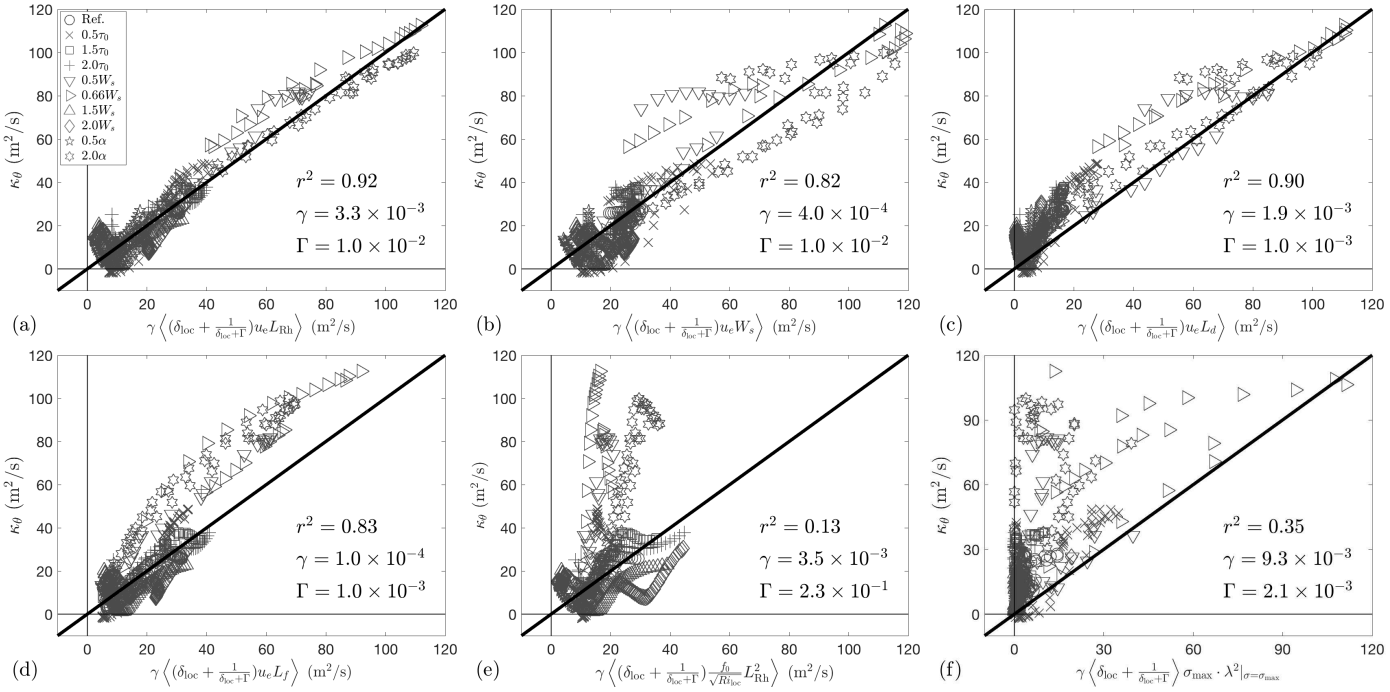

Figure 9: As Fig. 8, but with scalings adapted by $\delta-$dependent prefactors following (45). The correlation coefficients quoted in each panel are all statistically significant at the 1% level.

and found that a constant prefactor $\gamma = 0.015$ in (42) applied to a range of baroclinic processes. Over steep slopes, however, we found no optimal length scale for (42) after a series of tests (not shown). The topographic Rhines scale is thus chosen as a representative case. Fig. 8(e) shows that the local form of (42),

$$\kappa_{\mathrm{V97}} = \gamma \frac{f_0}{\sqrt{Ri_{\mathrm{loc}}}} L_{\mathrm{Rh}}^2, \tag{44}$$

is uncorrelated with the diagnosed diffusivity.

Under the Eady (1949) or Phillips (1954) model setup, κ_{S72} is equivalent to κ_{V97} if the deformation radius is used as the eddy length scale, since the most unstable mode resulting from the interacting surface and bottom edge waves has fixed wavelength proportional to the deformation radius (Vallis, 2006). In primitive equation simulations, however, the most unstable baroclinic mode is not necessarily excited by edge wave interactions, and its wavelength has to be diagnosed locally. In addition, lateral shear of the alongshore flow tends to modulate the linear wave characteristics (Killworth, 1980). We therefore conducted a linear stability analysis following the approach detailed in §4.4 of WS18 to extract the most unstable modes whose wavelength is at least half of the deformation radius at each latitude across the slope region. Expanding the search range in wavelength does not change the result. Fig. 8(f) shows that the Stone (1972) scaling is uncorrelated with the diagnosed eddy diffusivity.

3.4.2. Slope-aware mixing length theory-based scalings

We now adapt these tested MLT-based scalings to a sloping ocean bed by utilizing an empirical functional relation between the eddy buoyancy diffusivity and the local slope parameter that is similar to (19). Our proposed scaling follows

$$\kappa_{\mathrm{MLT}} = \gamma \left(\delta_{\mathrm{loc}} + \frac{1}{\delta_{\mathrm{loc}} + \Gamma} \right) u_e l_e. \tag{45}$$

Here γ is a constant prefactor and $\Gamma \ll 1$ can be adjusted so that γ/Γ reaches the same order of magnitude as the MLT scaling coefficient diagnosed over a flat ocean bed ($\delta_{\mathrm{loc}} = 0$). Equation (45) differs from (36) by a factor of $\delta_{\mathrm{loc}} + 1/(\delta_{\mathrm{loc}} + \Gamma)$, which, as we show in the following, significantly improves its predictive skill. We treat Jansen et al.'s (2015) diagnostics over a flat ocean bed (summarized in their Fig. 6) as a starting point to better frame the order of magnitude of Γ.

In Fig. 9(a), we plot the cross-slope eddy diffusivity κ_θ against the $\delta-$dependent MLT-based scaling using the topographic Rhines scale (16) and the eddy velocity (17),

$$\kappa_{\mathrm{MLT}} = \gamma F_{\mathrm{MLT}}(\delta_{\mathrm{loc}}) \cdot u_e L_{\mathrm{Rh}}, \tag{46a}$$

$$F_{\mathrm{MLT}}(\delta_{\mathrm{loc}}) = \delta_{\mathrm{loc}} + \frac{1}{\delta_{\mathrm{loc}} + \Gamma}, \tag{46b}$$

where $\gamma = 3.3 \times 10^{-3}$ is selected to optimize the linear fit between κ_{MLT} and κ_θ, and $\Gamma = 1.0 \times 10^{-2}$ simplifies (46) to $\kappa_{\mathrm{MLT}} = 0.33 u_e L_{\mathrm{Rh}}$ when $\delta_{\mathrm{loc}} \to 0$ (see Table 3). The prefactor then reaches the same order of magnitude as that diagnosed by Jansen et al. (2015). Importantly, the correlation achieved by κ_{MLT} against κ_θ ($r^2 = 0.92$) is much enhanced compared to the case shown in Fig. 8(a).

Next we replace the topographic Rhines scale in (46) with the slope half-width (Table 1) and plot the redefined κ_{MLT} against

κ_θ in Fig. 9(b). The prefactor $\gamma = 4.0 \times 10^{-4}$ is again chosen to optimize the diagnosis-scaling linear fit, which combined with $\Gamma = 1.0 \times 10^{-2}$ makes the prefactor asymptote to 4.0×10^{-2} in the flat bottom-limit, consistent with the value diagnosed by Jansen et al. (2015) when the "baroclinic width" was chosen as their eddy mixing length. The correlation between κ_θ and $\kappa_{\rm MLT}$ ($r^2 = 0.82$) slightly drops compared to the case shown in Fig. 9(a).

Over steep slopes, the topographic Rhines scale is comparable in magnitude to the first Rossby radius of deformation due to the suppressed eddy velocity scale and the increase of topographic PV gradient. In Fig. 9(c), we plot the relationship between the slope-aware $\kappa_{\rm MLT}$, with $L_{\rm Rh}$ substituted by L_d in (46), and the diagnosed eddy diffusivity. Here $\gamma = 1.9 \times 10^{-3}$ has the same order of magnitude as the prefactor when $L_{\rm Rh}$ serves as the mixing length. However, $\Gamma = 1.0 \times 10^{-3}$ makes the full coefficient of $\kappa_{\rm MLT}$ approach $O(1)$ in the flat-bottomed ocean, similar to the magnitude diagnosed by Jansen et al. (2015). The correlation is similarly strong ($r^2 = 0.90$) as in the case shown in Fig. 9(a).

Although we expect that the frictional scale to be less relevant over steep slopes, adopting L_f as the mixing length in (46) and assuming that $L_J = L_{\rm Rh}$ in (41) nevertheless yield a strong correlation between $\kappa_{\rm MLT}$ and κ_θ ($r^2 = 0.83$), as shown in Fig. 9(d). The prefactor has again been adjusted to optimize the diagnosis-scaling linear fit and to account for the magnitude of the MLT-based scaling reported by Jansen et al. (2015). The strong correlation does not imply that the eddy mixing is frictionally controlled over steep slopes, but rather that the local buoyancy frequency $\left(\int_{-|h|}^{0} N_s\, dz\right)\Big/|h|$ does not vary significantly (the variation is within a factor of 2 across the entire channel), leading to $L_f \sim L_{\rm Rh}$ based on (40)–(41).

Fig. 9(a)–(d) indicates that the scaling (45) is insensitive to the eddy length scale chosen over steep slopes, as long as the eddy velocity scale u_e is used. Implementation of (45) should therefore prioritize the optimal mixing length scale that makes the scaling transition smoothly from the slope toward the open ocean. If the diagnostics from the open ocean (both the shelf and the open ocean) are included in the comparison, the correlation of the Rhines scale-based $\kappa_{\rm MLT}$ (46) with the diagnosed diffusivity reduces to $r^2 = 0.79$ ($r^2 = 0.65$), as shown in Fig. 5(c). Defining the frictional length scale, which is partly dependent on the topographic Rhines scale, as the mixing length in (45) slightly modifies the diagnosis-scaling correlation: the correlation coefficient is $r^2 = 0.71$ if the open ocean is included and $r^2 = 0.52$ if both the shelf and the open ocean are included (not shown). In contrast, neither the deformation radius nor the slope half-width produces a diagnosis-scaling correlation better than $r^2 = 0.06$ if the open ocean diagnostics are included. Our findings therefore suggest that the Rhines scale is the most suitable choice for the eddy mixing length, mirroring findings of Jansen et al. (2015) in the context of a flat-bottomed ocean.

In Fig. 9(e)–(f) we also test the slope-aware forms of the local Visbeck et al. (1997) scaling

$$\kappa_{\rm V97} = \gamma F_{\rm MLT} \cdot \frac{f_0}{\sqrt{Ri_{\rm loc}}} L_{\rm Rh}^2, \tag{47}$$

and the local Stone (1972) scaling

$$\kappa_{\rm S72} = \gamma F_{\rm MLT} \cdot \sigma_{\rm max} \cdot \lambda^2|_{\sigma=\sigma_{\rm max}}. \tag{48}$$

These formulations do not show significant improvements in predictive skill compared to their slope-unaware counterparts. Our findings suggest that accurate implementation of the MLT-based scaling for steep slopes depends crucially on the subgrid EKE budget.

4. Impact of along-slope topographic variations

§3.2–§3.4 suggest that eddy buoyancy mixing across continental slopes can be reproduced via the GEOMETRIC scaling, the CF scaling, or the $\delta-$dependent MLT-based scaling that incorporates the eddy velocity scale u_e and the topographic Rhines scale $L_{\rm Rh}$. While both the GEOMETRIC scaling and the CF scaling are able to quantify the eddy transfer across steep slopes with suitably-chosen constant prefactors, they require δ-dependent prefactors to transition from the slope to the open ocean. In this section, we investigate the extent to which these slope-aware scaling frameworks apply to continental slopes featuring topographic canyons and ridges, over which standing meanders lead to stronger restratification, and the topographically induced prograde flows tend to penetrate to the upper ocean (*c.f.* §2.3).

4.1. Meridional vs cross-isobath eddy mixing

In the context of corrugated continental slope, we face a choice as whether to compare the scalings with the eddy buoyancy diffusivity directed across meridians (9a) or across isobaths (10a). To address this, we first assess the functional dependence of eddy diffusivity on the two most crucial nondimensional parameters over steep slopes: the local slope parameter and the local Richardson number (*c.f.* §3.1). There is some freedom in defining these two parameters in the presence of canyons/ridges because the mean geostrophic currents do not follow the isobaths (Fig. 1(b)). One choice would be to completely neglect the zonal variations in the topography and mean flow, and define these two parameters via the meridional components of the mean buoyancy and bathymetry gradients. However, the resulting $\delta_{\rm loc}$ and $Ri_{\rm loc}$ exhibit no correlation with the meridional eddy buoyancy transfer (not shown). Instead, we use the local slope parameter and the local Richardson number defined by (11) and (12), respectively. That is, we ignore the cross-isobath part of the mean flow, and assume that the eddy buoyancy transfer, either in the meridional direction or in the cross-isobath direction, is determined by the along-isobath component of the large-scale geostrophic current.

In Fig 10(a), we compare the *zonally averaged* slope parameter $\langle\delta_{\rm loc}\rangle$ with the *meridional* eddy buoyancy diffusivity κ_θ. Diagnostics have been drawn from three zonal regions across the channel: (i) the region peripheral to the northern/southern slope regions with ocean depths between 510 m and 3990 m and lying south of $y = 450$ km, (ii) the northern/southern slope regions, and (iii) the central slope region. Diagnostics from these regions have been plotted with light gray, dark gray, and blue

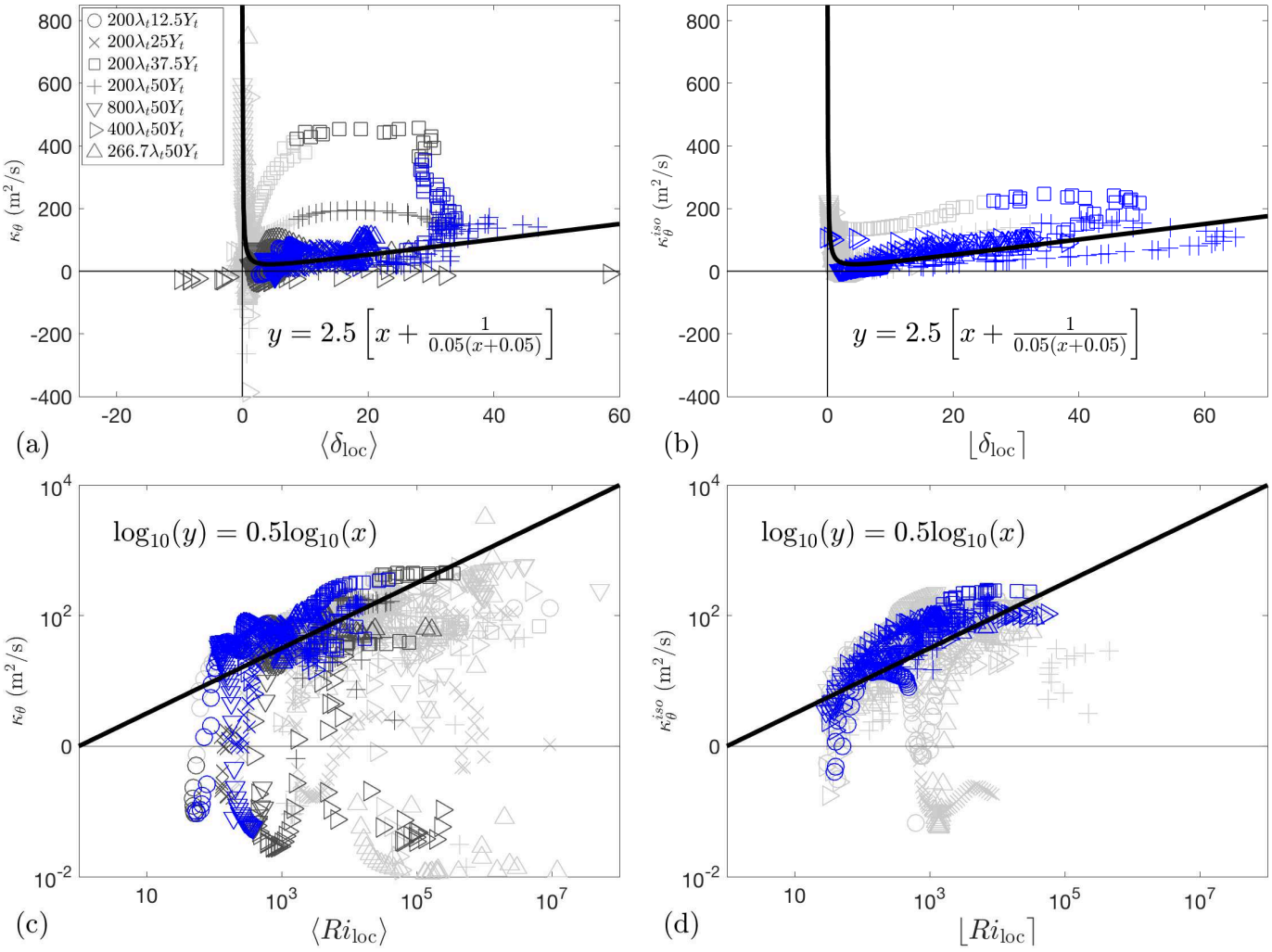

Figure 10: (a) Scatter plot of depth-averaged eddy buoyancy diffusivity in the meridional direction against the zonally averaged local slope parameter in the CORRUG runs. (b) Scatter plot of depth-averaged eddy buoyancy diffusivity in the cross-isobath direction against the along-isobath-averaged local slope parameter in the CORRUG runs. (c) Scatter plot of depth-averaged eddy buoyancy diffusivity in the meridional direction against the zonally averaged local Richardson number in the CORRUG runs. (d) Scatter plot of depth-averaged eddy buoyancy diffusivity in the cross-isobath direction against the along-isobath-averaged local Richardson number in the CORRUG runs. In panels (a) and (c), light gray markers indicate diagnostics made from the peripheral regions to the north (south) of the northern (southern) slope regions, dark gray markers indicate diagnostics made from the northern/southern slope regions, and blue markers indicate diagnostics made across the central slope regions (see text in §2.2 for definitions of these regions). In panels (b) and (d), light gray markers indicate diagnostics made from the peripheral regions of the slope with ocean depth $|h| \in$ [510 m, 938 m] or $|h| \in$ [3568 m, 3990 m], and blue markers indicate diagnostics made from the slope region with ocean depth $|h| \in$ [938 m, 3568 m] (see text in §4.1 for definitions of these regions). In panels (c) and (d), logarithmic axes are used to accommodate the wide range of the local Richardson number. The functional fit from Fig. 3(a) is presented in (a)–(b). The independent and dependent variables of the functional fits are represented by x and y in all panels, which should not be confused with the model domain coordinates.

markers, respectively. κ_θ exhibits a much more scattered relationship with $\delta_{\rm loc}$ than in the SMOOTH runs, shown in Fig. 3(a). The simple $\delta-$function fit (19) becomes limited in characterizing the variation of meridional mixing across corrugated slopes. Strongly negative diffusivities of $O(-100)$ m^2/s emerge on the peripheries of the continental slope, and slightly negative eddy diffusivity with negative values of $\langle\delta_{\rm loc}\rangle$ is found in the northern/southen slope regions. The negative values of $\langle\delta_{\rm loc}\rangle$ are due to stationary recirculations residing over topographic ridges.

In Fig. 10(b), we plot the cross-isobath eddy diffusivity κ_θ^{iso} defined by (10a) against the local slope parameter averaged along isobaths,

$$\lfloor\delta_{\rm loc}\rceil\,|_{\rm h=h_0} = \frac{\oint \delta_{\rm loc}\, ds}{\oint ds}. \tag{49}$$

Here $\lfloor\bullet\rceil$ denotes the along-isobath-mean operator and the line integral operator is performed where $h = h_0$. Diagnostics from the shelf and open ocean regions, defined by $|h| \in$ [510 m, 938 m] and $|h| \in$ [3568 m, 3990 m] respectively, are plotted with light gray markers, whereas the slope region, defined by $|h| \in$ [938 m, 3568 m], are plotted with blue markers. Our simulations show that the cross-isobath eddy diffusivity is in general smaller in magnitude than the meridional one, consistent with the example shown in Fig. 2. In addition, the cross-isobath eddy diffusivity appears to be better fit by our empirically-derived function of $\delta_{\rm loc}$ (19) than the meridional eddy diffusivity, indicating that the local slope parameter defined by (11) mainly constrains the cross-isobath, rather than meridional, component of transient eddy buoyancy fluxes.

In Figs. 10(c) and (d), we compare the relationship between the local Richardson number and the eddy diffusivity under a zonal vs along-isobath average, respectively. Over corrugated slopes, the local Richardson number reaches $O(10^2) - O(10^7)$ due to the stronger restratification and thus weaker baroclinic shear of the flow. The along-isobath-average calculation produces a better fit between the square root of the local Richard-

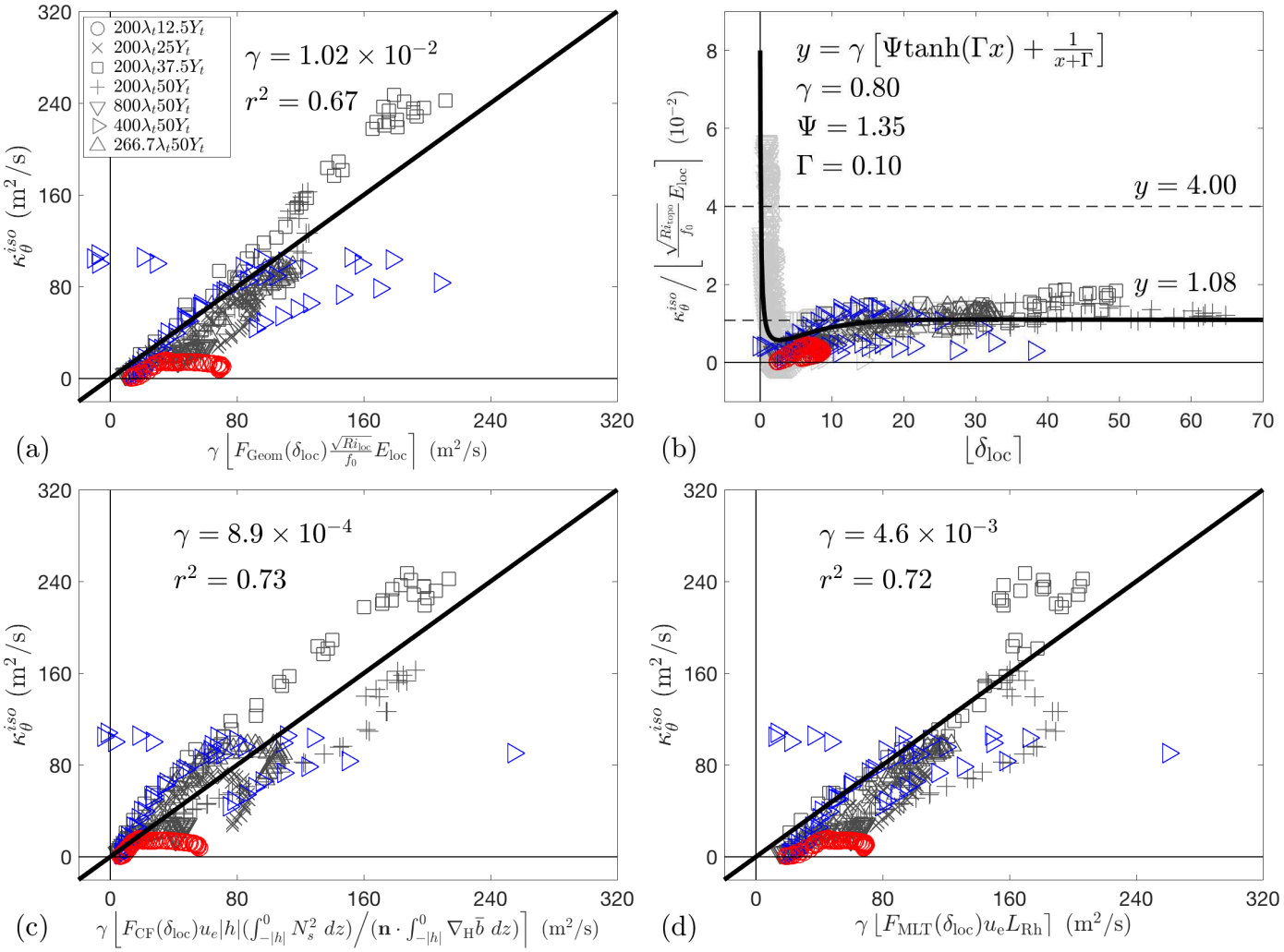

Figure 11: Scatter plots of the depth-averaged eddy buoyancy diffusivity in the cross-isobath direction derived from the CORRUG runs, against the slope-aware forms of (a) the local GEOMETRIC scaling, (c) the local CF scaling, and (d) the local MLT-based scaling, with constant coefficients γ selected to optimize the linear fits. Panel (b) illustrates the variation of the GEOMETRIC prefactor with the local slope parameter, superimposed by identical functional fit presented in Fig. 4(b). Dark gray markers indicate diagnostics drawn from the slope region defined by ocean depths in the range $|h| \in$ [938 m, 3568 m]. Light gray markers in panel (b) indicate diagnostics drawn from the peripheral regions of the slope, between sea floor depths of $|h| \in$ [510 m, 3990 m]. Red (blue) markers indicate diagnostics drawn from the slope region produced by the CORRUG_200λ_t12.5Y_t (CORRUG_400λ_t50Y_t) run. The functions $F_{\rm Geom}$, $F_{\rm CF}$, and $F_{\rm MLT}$ are given by (24b), (29b), and (46b), respectively, and are summarized in Table 3. The correlation coefficients quoted in each panel are all statistically significant at the 1% level. The independent and dependent variables of the functional fits are represented by x and y in panel (b), which should not be confused with the model domain coordinates.

son number

$$\lfloor Ri_{\rm loc} \rceil_{\rm h=h_0} = \frac{\oint Ri_{\rm loc} \, ds}{\oint ds} \tag{50}$$

and the eddy diffusivity κ_θ^{iso} than that produced by the zonal-average calculation.

4.2. *Scaling cross-isobath mixing over corrugated slopes*

In this section, we evaluate the predictive skills of the scalings proposed in §3.2–§3.4 over corrugated slopes. We compare these scalings under an along-isobath-average because our diagnostics in Fig. 10 indicate that the local eddy diffusivity has stronger functional relationships with the local slope parameter and the local Richardson number under an along-isobath-average than under a zonal average. Because the local slope parameter varies even *along* the isobaths of a corrugated slope due to the presence of standing eddies, the $\delta-$dependent prefactors for these scalings are preserved from §3 before the along-isobath-averages are made.

Fig. 11(a) shows the relationship between κ_θ^{iso} and the slope-aware GEOMETRIC scaling,

$$\kappa_{\rm Geom}^{\rm topo} = \gamma \left\lfloor F_{\rm Geom}(\delta_{\rm loc}) \frac{\sqrt{Ri_{\rm loc}}}{f_0} E_{\rm loc} \right\rceil, \tag{51}$$

in which the empirical function $F_{\rm Geom}$ is identical to (24b) (see Table 3 for selected values of parameters in $F_{\rm Geom}$), and $\gamma = 1.02 \times 10^{-2}$ is a constant chosen to optimize the linear fit between $\kappa_{\rm Geom}^{\rm topo}$ and κ_θ^{iso}. The diagnosis-scaling correlation ($r^2 = 0.67$) is smaller than for the case of zonally uniform slopes ($r^2 = 0.92$). A fraction of diagnosed diffusivities, such as those produced by CORRUG_200λ_t12.5Y_t (highlighted with red markers), and CORRUG_400λ_t50Y_t (highlighted with blue markers) are particularly poorly captured by (51). Negative values of $\kappa_{\rm Geom}^{\rm topo}$ in CORRUG_400λ_t50Y_t indicates the presence of locally prograde fronts (*i.e.* $\delta_{\rm loc} < 0$) associated with standing meanders.

In Fig. 11(b) we investigate the factors that contribute to

the diversion of diagnosed eddy diffusivity from the theoretical prediction by plotting the diagnosed GEOMETRIC prefactor against the local slope parameter, as in Fig. 4(b). This plot shows that the empirical relation between γ_{Geom} and δ_{loc} in the SMOOTH simulations approximately applies to the CORRUG simulations. However, as the ocean bed becomes steeper, the diagnosed prefactor exhibits more scatter in the CORRUG simulations than in the SMOOTH simulations. Specifically, for $\langle \delta_{\text{loc}} \rangle > 10$, the diagnosed GEOMETRIC prefactor ranges between [0.94, 1.84] in the SMOOTH simulations but between [0.06, 1.87] in the CORRUG simulations.

In Fig. 11(c) we plot κ_θ^{iso} against the slope-aware CF scaling,

$$\kappa_{\text{CF}}^{\text{topo}} = \gamma \left[F_{\text{CF}}(\delta_{\text{loc}}) u_e |h| \frac{\int_{-|h|}^{0} N_s^2 \, dz}{\left| \mathbf{n} \cdot \int_{-|h|}^{0} \nabla_{\text{h}} \overline{b} \, dz \right|} \right], \tag{52}$$

in which $\mathbf{n} = -\nabla_H h / |\nabla_H h|$, F_{CF} is identical to (29b) (see Table 3 for selected values of parameters in F_{CF}), and $\gamma = 8.9 \times 10^{-4}$ is selected to optimize the linear fit. The diagnosis-scaling correlation ($r^2 = 0.73$) is slightly stronger than that in Fig. 11(a), but remains weaker than for the case of zonally uniform slopes ($r^2 = 0.86$). As in the GEOMETRIC case, the weaker agreement between the diagnosed diffusivity and the scaling (52) shown in Fig. 11(c) is partly due to the outlying results from CORRUG_200λ_{t}12.5Y_{t} and CORRUG_400λ_{t}50Y_{t}.

In Fig. 11(d) we contrast κ_θ^{iso} against the slope aware MLT-based scaling

$$\kappa_{\text{MLT}}^{\text{topo}} = \gamma \lfloor F_{\text{MLT}}(\delta_{\text{loc}}) u_e L_{\text{Rh}} \rceil, \tag{53}$$

in which F_{MLT} is identical to (46b) (see Table 3 for selected value of parameter in F_{MLT}), and $\gamma = 4.6 \times 10^{-3}$ optimizes the linear fit. The diagnosis-scaling correlation ($r^2 = 0.72$) is comparable to those produced by the GEOMETRIC and the CF scalings. The weaker agreement between the diagnosed diffusivity and the scaling (53) contrasted to the SMOOTH case ($r^2 = 0.92$) is again partly attributed to the outlying results from CORRUG_200λ_{t}12.5Y_{t} and CORRUG_400λ_{t}50Y_{t}.

4.3. Cross-slope-averaged scaling of cross-slope eddy mixing

In the flat-bottomed ocean context, Jansen et al. (2015) proposed a parameterization using the bulk-averaged eddy mixing over an entire baroclinic zone, rather than using horizontally-local properties. This approach may also be favored over continental slopes, as topographic corrugation leads to increased scatter of the diagnosed eddy diffusivity against the scalings proposed in this study (see Fig. 11). In addition, WS18 have shown that the eddy energy transfer becomes non-local (*e.g.* Chen et al. 2014) across steep slopes, and any closure of the subgrid eddy energy, from which the eddy velocity is provided, based on the local production/dissipation balance (*e.g.* Cessi 2008) may become inaccurate. In Fig. 12, we plot the diagnosed cross-isobath eddy diffusivity $\{\kappa_\theta^{iso}\}$ against the three slope-aware scalings after averaging over the continental slope regions, defined by ocean depths in the range $|h| \in$ [938 m, 3568 m], where $\{\bullet\}$ denotes the bulk area-mean operator. Diagnostics from both the SMOOTH (black markers) and the CORRUG (blue markers) simulations are included. All three scalings produce strong correlations ($r^2 > 0.80$) with the diagnosed diffusivity across our suite of simulations. The bulk eddy transfer coefficients in the SMOOTH simulations are particularly closely reproduced, with correlations exceeding $r^2 = 0.89$, and reaching $r^2 = 0.98$ for the MLT case.

5. Discussion and conclusion

Accurate representation of mesoscale eddy effects in coarse-resolution ocean climate models remains a pressing challenge for the oceanographic community. Mid-latitude mesoscale eddies over continental slopes, in particular, cannot be resolved even in eddy-permitting global ocean models (Hallberg, 2013). Existing approaches of eddy parameterization have mostly been developed based on the open ocean turbulent properties and are thus independent of the bottom topography, which may lead to incorrect water mass formations and adjustment of ocean general circulations over continental slopes.

In this article, we have examined three numerically implementable scalings for eddy buoyancy transfer across retrograde slope fronts: the GEOMETRIC scaling originally developed by Marshall et al. (2012), a new Cross-Front scaling derived via dimensional analysis, and the mixing length theory (MTL)-based scaling (Prandtl, 1925). We demonstrate that both the GEOMETRIC framework and the CF scaling are capable of quantifying the eddy diffusivity over the continental slope, in isolation, following the selection of suitable constant prefactor coefficients. However, in order to capture the eddy mixing across both the continental slope and the open ocean, all three scaling approaches require the insertion of a prefactor that depends on the slope parameter δ.

We have shown that by making the prefactor a simple analytical function of the local slope parameter, each of these scalings is able to reproduce the depth-averaged eddy mixing over the slope and in the open ocean (*c.f.* Fig. 5). However, over continental shelves, the eddy transfer coefficients are much less well captured by these scalings. The reason for this is unclear and must be addressed in future work based on the studies focusing on continental shelves (*e.g.* Brink 2016). It should be noted that the continental shelves in our simulations are set to be unrealistically deep in order to isolate the cross-slope eddy fluxes, and therefore may have limited applicability to cross-shelf eddy fluxes.

Table 3 summarizes our proposed slope-aware scalings, with parameter values chosen based on our cross-slope-averaged calculation (Fig. 12), which maximizes the agreements between the scalings and the diagnosed eddy diffusivity. The prefactor for both the GEOMETRIC framework and the CF scaling can be constructed as the sum of a sigmoid function (*e.g.* hyperbolic tangent in this study) and a decay function (*e.g.* reciprocal function in this study) of the local slope parameter, which converge to empirical constants over the flat ocean bed and over steep slopes. For MLT-based scaling, we propose a linear function of δ_{loc} combined with a decay function. However, this function becomes unbounded if the isopycnals are completely flat

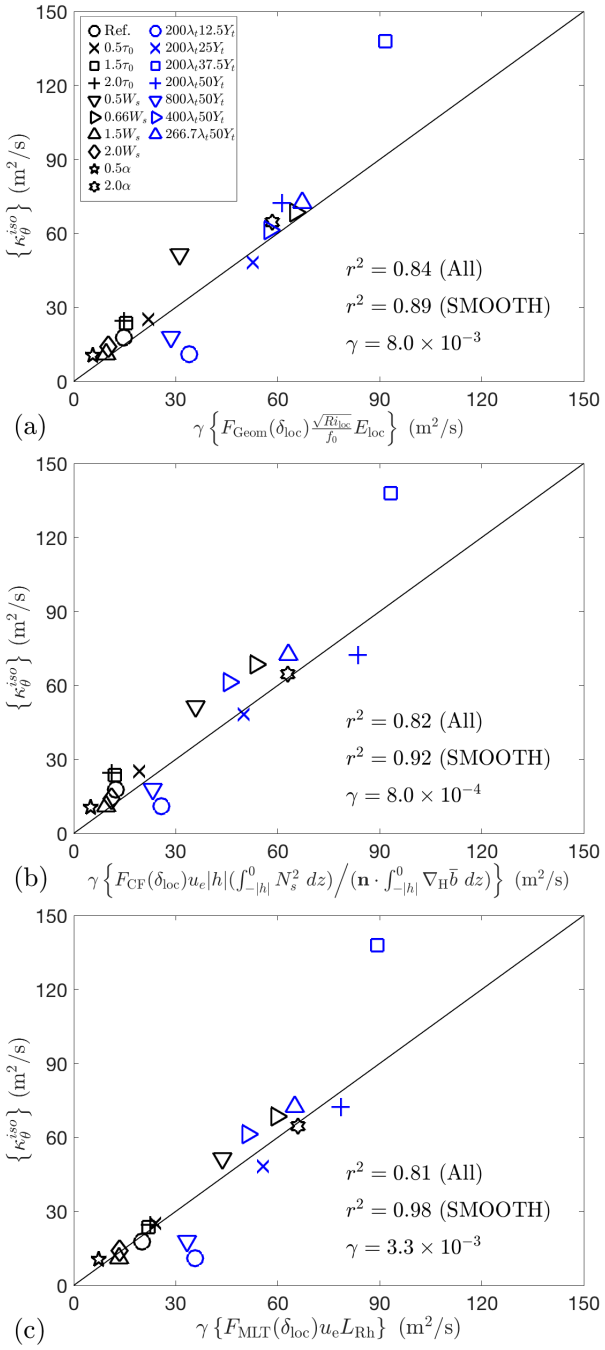

Figure 12: Scatter plots of the depth-averaged eddy buoyancy diffusivity in the cross-isobath direction against the slope-aware forms of (a) the local GEOMETRIC scaling, (b) the local CF scaling, and (c) the local MLT-based scaling, with constant γ selected to optimize the linear fits. Diagnostics are bulk-averaged across the continental slope region, defined by sea floor depths in the range $|h| \in$ [938 m, 3568 m], in both the SMOOTH and CORRUG runs. Black (blue) markers indicate diagnostics made from the SMOOTH (CORRUG) simulations. The functions F_{Geom}, F_{CF}, and F_{MLT} are given by (24b), (29b), and (46b), respectively, and summarized in Table 3. The correlation coefficients quoted in each panel are all statistically significant at the 1% level.

over the slope (*i.e.* $\delta_{\mathrm{loc}} \to +\infty$). For numerical implementation purposes, one can fix this issue by replacing the linear function with a nonlinear one that asymptotes to an empirical constant or decay to zero when the slope parameter crosses a threshold value. It should be noted that the sign of each slope-aware scaling depends not only on the sign of the local slope parameter, but also on the specific functional form of its prefactor. A scaling designed for retrograde front (*i.e.* $\delta_{\mathrm{loc}} > 0$) may thus stay positive when the slope parameter turns negative (see Fig. 11). This issue can be addressed by adding a switch-like heaviside function of δ_{loc} that shuts down the mixing across a retrograde front when δ_{loc} turns negative.

In the context of buoyancy-driven *prograde* front (*i.e.* $\delta_{\mathrm{loc}} < 0$), Spall (2004) has previously proposed a slope-dependent scaling for the eddy heat flux,

$$\overline{v'\theta'} \sim e^{-2|\delta_{\mathrm{loc}}|} \, U_{\mathrm{tw}} \cdot \Delta\bar{\theta}, \tag{54}$$

where $\Delta\bar{\theta}$ denotes the temperature (or buoyancy) difference across the front, whose spatial span can be approximated by the slope width. The scaling (54) was constructed to fit the analytical solution of eddy heat fluxes produced by the modified Eady (1949) model (Blumsack and Gierasch, 1972). Further rearrangement of (54) leads to

$$\kappa_\theta \sim e^{-2|\delta_{\mathrm{loc}}|} \, U_{\mathrm{tw}} \cdot W_s, \tag{55}$$

which constitutes a MLT-based scaling, posed in terms of the thermal wind velocity and the width of the slope. Spall's (2004) results combined with our findings complement existing eddy parameterizations by incorporating the leading order effects of bottom topography.

The substantially differing dynamics induced by bottom canyons/ridges limits the applicability of the slope-aware scalings developed based on eddy dynamics over zonally uniform slopes. For instance, our proposed scalings conceal the vertical structure of eddy mixing, which may substantially impact the along-slope flow in the presence of topographic corrugations. This is reflected in Fig. 1(c)–(d): even slight bottom corrugation tends to expand the region occupied by topographically induced prograde flows. Notwithstanding these issues, our recommended slope-aware scalings produce much stronger correlations with the diagnosed cross-isobath eddy diffusivity over *corrugated slopes* compared with those between the topography-independent eddy parameterizations and diagnosed eddy transfer coefficients over *zonally uniform* slopes. This indicates that adaption of existing eddy parameterizations via the $\delta-$functions is a promising avenue for future model development efforts.

Parameterizing standing eddy effects over large-scale topographic features remain an open challenge in physical oceanography. Though our scalings do not predict the standing eddy component of cross-slope buoyancy flux, they constitute a significant step toward parameterizing the transient component of cross-slope buoyancy mixing and thus should be tested as parameterizations in coarse-resolution models. It is particularly important to investigate whether a coarse resolution model that can resolve large-scale bathymetric variations, but not transient eddy generation, will be able to represent the standing eddy buoyancy fluxes across continental slopes. Such an investigation may be more pertinent to eddy-permitting global ocean

models (*e.g.* Uchida et al. 2017). Indeed, for typical IPCC-Class Earth System Models with horizontal grid spacing of 1^o or coarser, even the continental shelf/slope itself may be unresolved. If eddy-permitting models can indeed reproduce standing eddy fluxes, a parameterization of the transient eddy buoyancy flux would be the only part that is required to represent the mesoscale.

To convert our proposed scalings into full closures of transient eddy buoyancy fluxes, *a priori* knowledge of the EKE or the total eddy energy is required. Modern ocean general circulation models such as the MOM6 are increasingly maintaining prognostic subgrid EKE or total eddy energy budgets (*e.g.* Jansen et al. 2019; Mak et al. 2018). These models will serve as a natural starting point for testing slope-aware eddy parameterizations. However, caution must taken, given that most subgrid eddy energy budgets only reflect open ocean eddy properties. Over continental slopes, lateral EKE fluxes via anomalous pressure work are dominant in the upper ocean, and EKE tends to be converted into potential energy near the ocean bed (WS18), both of which remain poorly constrained by existing eddy parameterizations (*e.g.* Eden and Greatbatch 2008; Maltrud and Holloway 2008)[5]. In addition, parameterization of eddy energy dissipation near topographic features remains a challenging research topic even for the well-studied open ocean (*e.g.* Yang et al. 2018). To accurately apply our proposed scalings, existing formulations of subgrid EKE budgets may need to be adapted to steep continental slopes.

Though the slope-aware scalings exhibit remarkable skill in quantifying the depth-averaged cross-slope eddy buoyancy transfer, our idealized model configuration carries several caveats. For instance, we did not consider the effects of external buoyancy forcing, which can considerably modulate the structure of slope fronts (*e.g.* Stewart and Thompson 2013). Time-dependent wind forcing can also project onto mesoscale variability over steep slopes (*e.g.* Zhai and Greatbatch 2007; Renault et al. 2016), and the evolution to equilibrium may be substantially modulated by "eddy memory" (Sinha and Abernathey, 2016; Manucharyan et al., 2017; Manucharyan and Isachsen, 2019). Tidal flows, which have been completely neglected in this study, may play a critical role in shaping the shelf break fronts (Brink, 2012, 2013). Our study has focused on the cross-slope eddy buoyancy transfer, and it remains unclear how closely this is related to the isopycnal eddy mixing (Redi, 1982). In the context of a flat-bottomed ocean, Abernathey et al. (2013) derived an analytical relation (their Equation (24)) between the GM and the Redi eddy transfer coefficients. The merits of this relation in inferring the isopycnal diffusivity via the GM transfer coefficient, particularly over continental slopes, have yet to be investigated. All these issues remain to be addressed in future investigations.

[5]Maltrud and Holloway (2008) and related work have proposed to implement a biharmonic or Laplacian viscosity that forces a mean prograde flow along the isobaths of a continental slope, thus ensembling the eddy-rectified flow character. However, this approach is not energetically constrained.

Acknowledgement

YW and ALS were supported by National Science Foundation, grant numbers OCE-1538702 and OCE-1751386. YW acknowledges the support from the Hong Kong Branch of Southern Marine Science and Engineering Guangdong Laboratory (Guangzhou) (SMSEGL20SC01). This work used the Extreme Science and Engineering Discovery Environment (XSEDE, Towns et al. 2014), which is supported by National Science Foundation grant number ACI-1548562. Constructive remarks from two anonymous reviewers significantly improved this article.

Appendix A. Vertical structure of eddy mixing

Fig. 13(a) shows the cross-isobath eddy diffusivity of buoyancy averaged along each isobath of the slope regions ($|h| \in$ [938 m, 3568 m]) in the SMOOTH_Reference and the CORRUG_200λ_t12.5Y_t runs as functions of depth. In both simulations, mixing is surface-intensified and eddies are found to flux buoyancy up-gradient approaching the sloping ocean bed. The negative buoyancy diffusivity mirrors the formation of bottom-trapped prograde flows in Fig. 1(a)–(b). In Fig. 13(b), we switch the vertical coordinate from depth to the normalized height from the ocean bed by the Prandlt e-folding scale (*e.g.*Treguier and McWilliams 1990) defined in (41) with L_J approximated by the topographic Rhines scale. The exact locations of sign reversal of buoyancy diffusivity do not follow a clear trend with the normalized height, but are generally within πL_e from the sloping ocean bed.

Appendix B. Additional parameter dependence of eddy buoyancy diffusivity

The relation between $\langle Bu_{\rm loc}\rangle$ and κ_θ is illustrated in Fig. 14(a). The eddy diffusivity rapidly decreases as the slope Burger number increases from 0. Over continental slopes, however, κ_θ is rather insensitive to $\langle Bu_{\rm loc}\rangle$. These can be understood via the relationships of $\langle\delta_{\rm loc}\rangle$ and $\langle Ri_{\rm loc}\rangle$ to the cross-slope eddy diffusivity. In the nearly flat-bottomed ocean, we have $\kappa_\theta \sim \gamma_1 \langle\delta_{\rm loc}\rangle^{-1}$ (Fig. 3(a)) and $\kappa_\theta \sim \gamma_2 \left\langle 10^{-3}\, Ri_{\rm loc}\right\rangle^{1/2}$ (Fig. 3(b)), where $\gamma_1 \simeq 50$ and $\gamma_2 \in [-1,\ 350]$, then (15) leads to $\kappa_\theta \sim 10^{-3/4}(50\gamma_2)^{1/2}\langle Bu_{\rm loc}\rangle^{-1/2}$. In Fig. 14(a) we plot the corresponding functional fit for $\gamma_2 = 1$ ($\gamma_2 = 350$) in solid (dashed) line, which captures the rapid decay of eddy mixing with the slope Burger number. As the ocean bed becomes steeper, we have $\kappa_\theta \sim \gamma_1 \langle\delta_{\rm loc}\rangle$ (Fig. 3(a)) and $\kappa_\theta \sim \gamma_2 \left\langle 10^{-3}\, Ri_{\rm loc}\right\rangle^{1/2}$ (Fig. 3(b)), then (15) gives $\langle Bu_{\rm loc}\rangle \simeq 0.95$ for $\gamma_1 = 2.5$ and $\gamma_2 = 75$, which provides no information about the eddy diffusivity. That is, the eddy diffusivity is almost independent of the slope Burger number over steep slopes in retrograde fronts.

Fig. 14(b) contrasts the topographic Rhines scale $\langle L_{\rm Rh}\rangle$ with the cross-slope eddy diffusivity. We fit a weakly quadratic relation, which produces a least-squares error slightly smaller than that generated by an optimized linear fit (by a factor of approximately 1.2) when diagnostics from the continental slope and

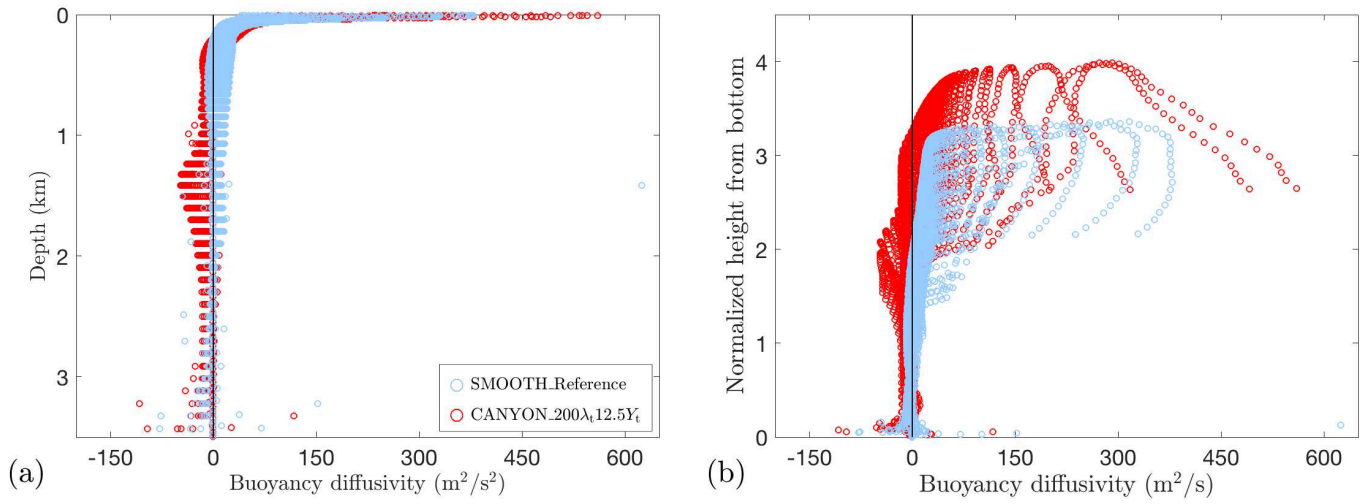

Figure 13: The cross-isobath eddy buoyancy diffusivity across the continental slope regions defined by ocean depths in the range $|h| \in$ [938 m, 3568 m] as functions of (a) depth and (b) normalized height from the ocean bed by the Prandlt $e-$folding scale defined in (41). Diagnostics are averaged along isobaths. Blue (red) markers indicate diagnostics from the SMOOTH_Reference (CORRUG_200λ_t12.5Y_t) run.

the open ocean are considered. The quadratic approximation is no better than a linear fit when the continental shelf is also included. Over the continental slope alone, no clear correlation between the two quantities is found. Comparing κ_θ against the first Rossby radius of deformation, or the Rhines scale normalized by the deformation radius, does not yield further insight (not shown).

We plot the depth-averaged EKE and EPE against the eddy diffusivity in Figs. 14(d) and (e), respectively. The two energy reservoirs are roughly equipartitioned with the local EPE slightly higher the local EKE. The strength of the cross-slope eddy mixing does not seem to be controlled by the amount of eddy energy alone. Indeed, over continental slopes, κ_θ is generally below 120 m^2/s, while neither the EKE nor the EPE are generally lower than that in regions away from the slope.

References

Abernathey, R., Cessi, P., 2014. Topographic enhancement of eddy efficiency in baroclinic equilibration. J. Phys. Oceanogr. 44 (8), 2107–2126.

Abernathey, R., Ferreira, D., Klocker, A., 2013. Diagnostics of isopycnal mixing in a circumpolar channel. Ocean Modell. 72, 1–16.

Aiki, H., Zhai, X., Greatbatch, R. J., 2016. Energetics of the global ocean: The role of mesoscale eddies. Ch. 4, pp. 109–134.

Allen, J. S., 1975. Coastal trapped waves in a stratified ocean. J. Phys. Oceanogr. 5 (2), 300–325.

Allen, S. E., Hickey, B. M., 2010. Dynamics of advection-driven upwelling over a shelf break submarine canyon. J. Geophys. Res. 115 (C8).

Bachman, S., Fox-Kemper, B., 2013. Eddy parameterization challenge suite I: Eady spindown. Ocean Model. 64, 12 – 28.

Bachman, S., Marshall, D., Maddison, J., Mak, J., 2017. Evaluation of a scalar eddy transport coefficient based on geometric constraints. Ocean Modell. 109, 44 – 54.

Bischoff, T., Thompson, A. F., 2014. Configuration of a Southern Ocean storm track. J. Phys. Oceanogr. 44 (12), 3072–3078.

Blumsack, S. L., Gierasch, P. J., 1972. Mars: The effects of topography on baroclinic instability. J. Atmos. Sci. 29 (6), 1081–1089.

Bower, A. S., Rossby, H. T., Lillibridge, J. L., 1985. The Gulf Stream—barrier or blender? J. Phys. Oceanogr. 15, 24–32.

Brink, K. H., 1986. Topographic drag due to barotropic flow over the continental shelf and slope. J. Phys. Oceanogr. 16 (12), 2150–2158.

Brink, K. H., 1991. Coastal-trapped waves and wind-driven currents over the continental shelf. Ann. Rev. Fluid Mech. 23 (1), 389–412.

Brink, K. H., 2010. Topographic rectification in a forced, dissipative, barotropic ocean. J. Mar. Res. 68 (3-4), 337–368.

Brink, K. H., 2011. Topographic rectification in a stratified ocean. J. Mar. Res. 69 (4-5), 483–499.

Brink, K. H., 2012. Baroclinic instability of an idealized tidal mixing front. J. Mar. Res. 70 (4), 661–688.

Brink, K. H., 2013. Instability of a tidal mixing front in the presence of realistic tides and mixing. J. of Mar. Res. 71 (3), 227–251.

Brink, K. H., 2016. Cross-shelf exchange. Annu. Rev. Fluid Mech. 8, 59–78.

Cacchione, D. A., Pratson, L. F., Ogston, A. S., 2002. The shaping of continental slopes by internal tides. Science 296 (5568), 724–727.

Cessi, P., 2008. An energy-constrained parameterization of eddy buoyancy flux. J. Phys. Oceanogr. 38 (8), 1807–1819.

Chelton, D. B., deSzoeke, R. A., Schlax, M. G., El Naggar, K., Siwertz, N., 1998. Geographical variability of the first baroclinic Rossby radius of deformation. J. Phys. Oceanogr. 28, 433–460.

Chen, R., Flierl, G. R., Wunsch, C., 2014. A description of local and nonlocal eddy-mean flow interaction in a global eddy-permitting state estimate. J. Phys. Oceanogr. 44 (9), 2336–2352.

Cherian, D. A., Brink, K. H., 2018. Shelf flows forced by deep-ocean anticyclonic eddies at the shelf break. J. Phys. Oceanogr. 48 (5), 1117–1138.

Colas, F., Capet, X., McWilliams, J. C., Li, Z., 2013. Mesoscale eddy buoyancy flux and eddy-Induced circulation in Eastern Boundary Currents. J. Phys. Oceanogr. 43 (6), 1073–1095.

Connolly, T. P., Hickey, B. M., Shulman, I., Thomson, R. E., 2014. Coastal trapped waves, alongshore pressure gradients, and the California Undercurrent. J. Phys. Oceanogr. 44 (1), 319–342.

Csanady, G. T., 1978. The arrested topographic wave. J. Phys. Oceanogr. 8 (1), 47–62.

Dinniman, M. S., Klinck, J. M., Jr., W. O. S., 2011. A model study of Circumpolar Deep Water on the West Antarctic Peninsula and Ross Sea continental shelves. Deep Sea Res. Pt. II 58 (13-16), 1508– 1523.

Eady, E. T., 1949. Long waves and cyclone waves. Tellus 1, 33–52.

Eden, C., 2007. Eddy length scales in the North Atlantic Ocean. J Geophys. Res. 112 (C6).

Eden, C., Greatbatch, R. J., 2008. Towards a mesoscale eddy closure. Ocean Model. 20 (3), 223 – 239.

Ferrari, R., Griffies, S. M., Nurser, A. G., Vallis, G. K., 2010. A boundary-value problem for the parameterized mesoscale eddy transport. Ocean Model. 32 (3), 143 – 156.

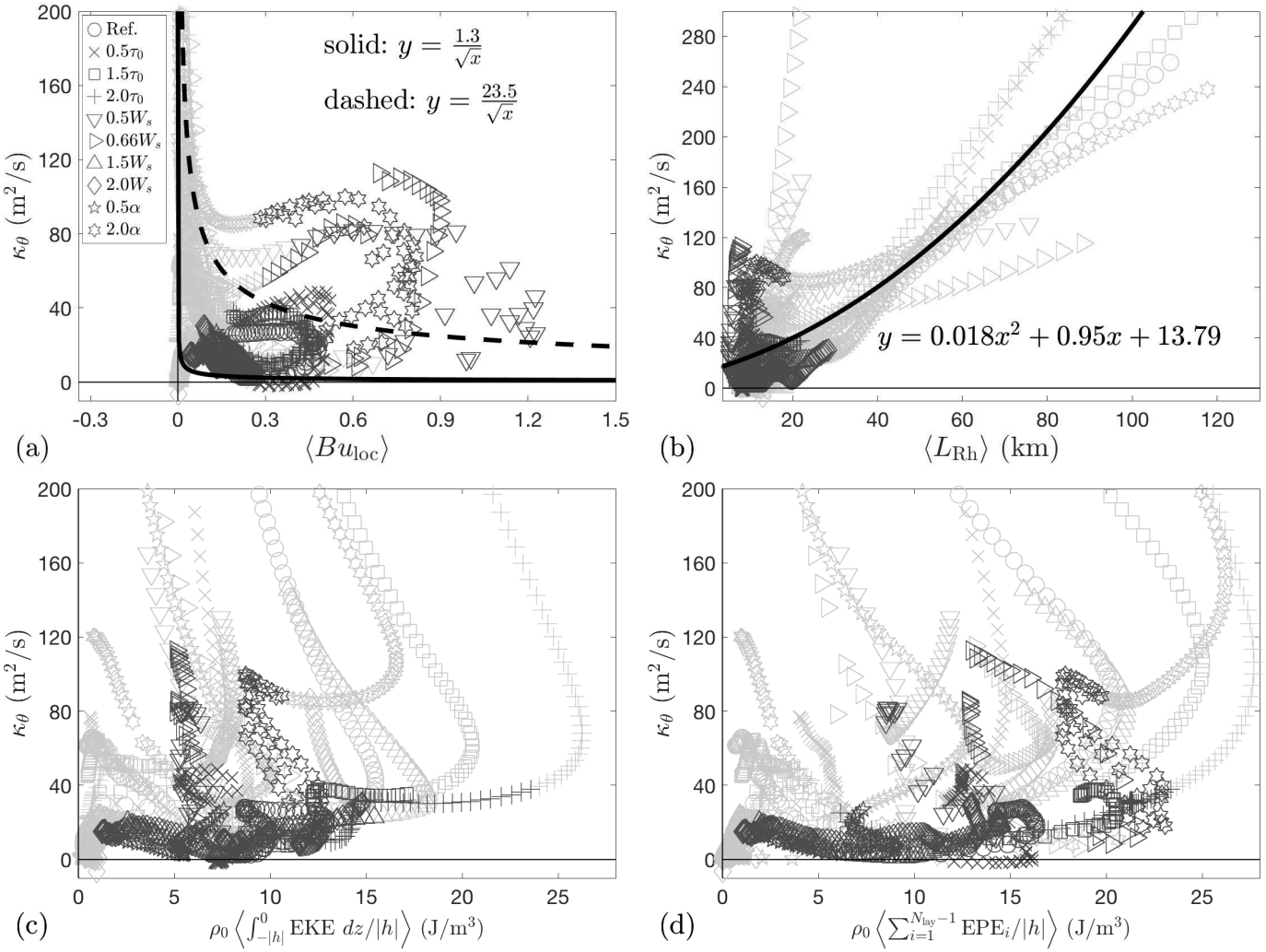

Figure 14: Scatter plots of the depth-averaged eddy buoyancy diffusivity against (a) the local slope Burger number, (b) the topographic Rhines scale calculated via the depth-averaged eddy kinetic energy, (c) the depth-averaged eddy kinetic energy density per unit area, and (d) the depth-averaged eddy potential energy density per unit area (See text in §3.1 for definitions of these parameters). All diagnostics are zonally averaged. Dark gray markers indicate diagnostics made over the slope, and light gray markers indicate the diagnostics made from the peripheral regions of the slope (see §3.1 for definitions of different regions). Selected functional fits have been overlaid to quantify the relations between the physical parameters and the local eddy buoyancy diffusivity. The independent and dependent variables of the functional fits are represented by x and y in panels (a)–(b), which should not be confused with the model domain coordinates.

Fox-Kemper, B., Danabasoglu, G., Ferrari, R., Griffies, S., Hallberg, R., Holland, M., Maltrud, M., Peacock, S., Samuels, B., 2011. Parameterization of mixed layer eddies. III: Implementation and impact in global ocean climate simulations. Ocean Model. 39 (1), 61 – 78.

Fox-Kemper, B., Ferrari, R., Hallberg, R., 2008. Parameterization of mixed layer eddies. Part I: Theory and diagnosis. J. Phys. Oceanogr. 38 (6), 1145–1165.

Fox-Kemper, B., Ferrari, R., Pedlosky, J., 2003. On the indeterminacy of rotational and divergent eddy fluxes. J. Phys. Oceanogr. 33 (2), 478–483.

Gan, J., Cheung, A., Guo, X., Li, L., 2009. Intensified upwelling over a widened shelf in the northeastern South China Sea. J. Geophys. Res. 114 (C9).

Gan, J., Ho, S. H., Liang, L., 2013. Dynamics of intensified downwelling circulation over a widened shelf in the northeastern South China Sea. J Phys. Oceanogr. 43 (1), 80–94.

Gent, P. R., McWilliams, J. C., 1990. Isopycnal mixing in ocean circulation models. J. Phys. Oceanogr. 20 (1), 150–155.

Ghaffari, P., Isachsen, P. E., Nøst, O. A., Weber, J. E., 2018. The influence of topography on the stability of the Norwegian Atlantic Current off northern Norway. J. Phys. Oceanogr. 48 (11), 2761–2777.

Green, J. S., 1970. Transfer properties of the large-scale eddies and the general circulation of the atmosphere. Quart. J. Roy. Meteor. Soc. 96, 157–185.

Griffies, S., 2004. Fundamentals of Ocean Climate Models. Princeton University Press.

Griffies, S. M., Böning, C., Bryan, F. O., Chassignet, E. P., Gerdes, R., Hasumi, H., Hirst, A., Treguier, A., Webb, D., 2000. Developments in ocean climate modelling. Ocean Modell. 2, 123–192.

Hallberg, R., 2013. Using a resolution function to regulate parameterizations of oceanic mesoscale eddy effects. Ocean Modell. 72, 92–103.

Harris, P. T., Whiteway, T., 2011. Global distribution of large submarine canyons: Geomorphic differences between active and passive continental margins. Mar. Geo. 285 (1), 69 – 86.

Hattermann, T., Smedsrud, L. H., Nst, O. A., Lilly, J. M., Galton-Fenzi, B. K., 2014. Eddy-resolving simulations of the Fimbul Ice Shelf cavity circulation: Basal melting and exchange with open ocean. Ocean Modell. 82, 28–44.

Hetland, R. D., 2017. Suppression of baroclinic instabilities in buoyancy-driven flow over sloping bathymetry. J. Phys. Oceanogr. 47 (1), 49–68.

Isachsen, P. E., 2011. Baroclinic instability and eddy tracer transport across sloping bottom topography: How well does a modified Eady model do in primitive equation simulations? Ocean Modell. 39 (1-2), 183–199.

Jansen, M. F., Adcroft, A., Khani, S., Kong, H., 2019. Toward an energetically consistent, resolution aware parameterization of ocean mesoscale eddies. J. Adv. Model. Earth Sys.

Jansen, M. F., Adcroft, A. J., Hallberg, R., Held, I. M., 2015. Parameterization of eddy fluxes based on a mesoscale energy budget. Ocean Model. 92, 28 – 41.

Jungclaus, J. H., Mellor, G. L., 2000. A three-dimensional model study of the Mediterranean outflow. J. Marine Sys. 24 (1-2), 41 – 66.

Kämpf, J., 2007. On the magnitude of upwelling fluxes in shelf-break canyons. Cont. Shelf Res. 27 (17), 2211 – 2223.

Killworth, P., 1980. Barotropic and baroclinic instability in rotating stratified fluids. Dyn. Atmos. Oceans 4, 143–184.

LaCasce, J. H., 1998. A geostrophic vortex over a slope. J. Phys. Oceanogr. 28 (12), 2362–2381.

LaCasce, J. H., 2017. The prevalence of oceanic surface modes. Geophys. Res.

Lett. 44 (21), 11,097–11,105.
LaCasce, J. H., Brink, K. H., 2000. Geostrophic turbulence over a slope. J. Phys. Oceanogr. 30 (6), 1305–1324.
LaCasce, J. H., Escartin, J., Chassignet, E. P., Xu, X., 2019. Jet instability over smooth, corrugated, and realistic bathymetry. J. Phys. Oceanogr. 49 (2), 585–605.
Large, W. G., McWilliams, J. C., Doney, S. C., 1994. Oceanic vertical mixing: A review and a model with a nonlocal boundary layer parameterization. Rev. Geophys. 32, 363–403.
Mak, J., Maddison, J. R., Marshall, D. P., Munday, D. R., 2018. Implementation of a geometrically informed and energetically constrained mesoscale eddy parameterization in an ocean circulation model. J. Phys. Oceanogr. 48 (10), 2363–2382.
Mak, J., Marshall, D., Maddison, J., Bachman, S., 2017. Emergent eddy saturation from an energy constrained eddy parameterisation. Ocean Model. 112, 125 – 138.
Maltrud, M., Holloway, G., 2008. Implementing biharmonic Neptune in a global eddying ocean model. Ocean Modelling 21 (1), 22 – 34.
Maltrud, M. E., Vallis, G. K., 1991. Energy spectra and coherent structures in forced two-dimensional and beta-plane turbulence. J. Fluid Mech. 228, 321–342.
Maltrud, M. E., Vallis, G. K., 1992. Generation of mean flow and jets on a Beta plane and over topography. J. Phys. Oceanogr. 23, 1346–1362.
Manucharyan, G. E., Isachsen, P. E., 2019. Critical Role of Continental Slopes in Halocline and Eddy Dynamics of the Ekman-Driven Beaufort Gyre. J Geophys. Res. 124 (4), 2679–2696.
Manucharyan, G. E., Thompson, A. F., Spall, M. A., 2017. Eddy memory mode of multidecadal variability in residual-mean ocean circulations with application to the Beaufort Gyre. J. Phys. Oceanogr. 47 (4), 855–866.
Marshall, D. P., Maddison, J. R., Berloff, P. S., 2012. A framework for parameterizing eddy potential vorticity fluxes. J. Phys. Oceanogr. 42, 539–557.
Marshall, J., Adcroft, A., Hill, C., Perelman, L., Heisey, C., 1997. A finite-volume, incompressible Navier Stokes model for studies of the ocean on parallel computers. J. Geophys. Res. 102 (C3), 5753–5766.
Marshall, J., Shutts, G., 1981. A note on rotational and divergent eddy fluxes. J. Phys. Oceanogr. 11 (12), 1677–1680.
Mechoso, C. R., 1980. Baroclinic instability of flows along sloping boundaries. J. Atmos. Sci. 37 (6), 1393–1399.
Merryfield, W. J., Holloway, G., 1999. Eddy fluxes and topography in stratified quasi-geostrophic models. J. Fluid Mech. 380, 59–80.
Nøst, O. A., Biuw, M., Tverberg, V., Lydersen, C., Hattermann, T., Zhou, Q., Smedsrud, L. H., Kovacs, K. M., 2011. Eddy overturning of the Antarctic Slope Front controls glacial melting in the Eastern Weddell Sea. J. Geophys. Res. 116 (C11).
Olascoaga, M. J., Rypina, I. I., Brown, M. G., Beron-Vera, F. J., Koçak, H., Brand, L. E., Halliwell, G. R., Shay, L. K., 2006. Persistent transport barrier on the West Florida Shelf. Geophys. Res. Lett. 33, L22603.
Pedlosky, J., 1987. Geophysical Fluid Dynamics, 2nd Edition. Springer.
Pennel, R., Stegner, A., Béranger, K., 2012. Shelf impact on buoyant coastal current instabilities. J. Phys. Oceanogr. 42 (1), 39–61.
Phillips, N., 1951. A simple three-dimensional model for the study of large-scale extratropical flow patterns. J. Atmos. Sci. 8, 381–394.
Phillips, N. A., 1954. Energy transformations and meridional circulations associated with simple baroclinic waves in a two -level quasi-geostrophic model. Tellus 6, 273–286.
Pickart, R. S., Spall, M. A., 2007. Impact of Labrador Sea Convection on the North Atlantic Meridional Overturning Circulation. J. Phys. Oceanogr. 37 (9), 2207–2227.
Poulin, F. J., Stegner, A., Hernández-Arencibia, M., Marrero-Díaz, A., Sangrà, P., 2014. Steep shelf stabilization of the coastal Bransfield Current: Linear stability analysis. J. Phys. Oceanogr. 44, 714–732.
Prandtl, L., 1925. Bericht ber untersuchungen zur ausgebildeten turbulenz. Zeitschr. Angew. Math. Mech. 5 (2), 136–139.
Redi, M. H., 1982. Oceanic isopycnal mixing by coordinate rotation. J. Phys. Oceanogr. 12 (10), 1154–1158.
Renault, L., Molemaker, M. J., McWilliams, J. C., Shchepetkin, A. F., Lemari, F., Chelton, D., Illig, S., Hall, A., 2016. Modulation of wind work by oceanic current interaction with the atmosphere. J. Phys. Oceanogr. 46 (6), 1685–1704.
Rhines, P., 1970. Edge-, bottom-, and Rossby waves in a rotating stratified fluid. Geophys. Astrophys. Fluid Dyn. 1, 273–302.
Serra, N., Ambar, I., 2002. Eddy generation in the Mediterranean undercurrent. Deep Sea Res. Pt. II 49 (19), 4225 – 4243.
Sinha, A., Abernathey, R. P., 2016. Time scales of Southern Ocean eddy equilibration. J. Phys. Oceanogr. 46 (9), 2785–2805.
Spall, M. A., 2004. Boundary currents and watermass transformation in marginal seas. J. Phys. Oceanogr. 34 (5), 1197–1213.
Spall, M. A., 2010. Dynamics of downwelling in an eddy-resolving convective basin. J. Phys. Oceanogr. 40 (10), 2341–2347.
Stevens, D. P., Ivchenko, V. O., 1997. The zonal momentum balance in an eddy-resolving general-circulation model of the Southern Ocean. Q. J. Royal Meteorol. Soc. 123 (540), 929–951.
Stewart, A. L., Hogg, A. M., 2017. Reshaping the Antarctic Circumpolar Current via Antarctic Bottom Water export. J. Phys. Oceanogr. 47 (10), 2577–2601.
Stewart, A. L., Thompson, A. F., 2012. Sensitivity of the ocean's deep overturning circulation to easterly Antarctic winds. Geophys. Res. Lett. 39 (18), L18604.
Stewart, A. L., Thompson, A. F., 2013. Connecting Antarctic cross-slope exchange with Southern Ocean overturning. J. Phys. Oceanogr. 43, 1453–1471.
Stewart, A. L., Thompson, A. F., 2015. The Neutral Density Temporal Residual Mean overturning circulation. Ocean Modelling 90, 44–56.
Stewart, A. L., Thompson, A. F., 2016. Eddy generation and jet formation via dense water outflows across the Antarctic continental slope. J. Phys. Oceanogr. 46, 3729–3750.
Stewart, K. D., Hogg, A. M., Griffies, S. M., Heerdegen, A. P., Ward, M. L., Spence, P., England, M. H., 2017. Vertical resolution of baroclinic modes in global ocean models. Ocean Modell. 113, 50–65.
Stone, P. H., 1972. A simplified radiative-dynamical model for the static stability of rotating atmospheres. J. Atmos. Sci. 29, 405–418.
Thompson, A. F., 2010. Jet formation and evolution in baroclinic turbulence with simple topography. J. Phys. Oceanogr. 40, 257–278.
Thompson, A. F., Naveira Garabato, A. C., 2014. Equilibration of the Antarctic Circumpolar Current by standing meanders. J. Phys. Oceanogr. 44 (7), 1811–1828.
Towns, J., Cockerill, T., Dahan, M., Foster, I., Gaither, K., Grimshaw, A., Hazlewood, V., Lathrop, S., Lifka, D., Peterson, G. D., Roskies, R., Scott, J. R., Wilkins-Diehr, N., Sept 2014. XSEDE: Accelerating scientific discovery. Computing in Science Engineering 16 (5), 62–74.
Treguier, A. M., McWilliams, J. C., 1990. Topographic influences on wind-driven, stratified flow in a beta-plane channel: An idealized model for the Antarctic Circumpolar Current. J. Phys. Oceanogr. 20 (3), 321–343.
Trodahl, M., Isachsen, P. E., 2018. Topographic influence on baroclinic instability and the mesoscale eddy field in the Northern North Atlantic Ocean and the Nordic Seas. J. Phys. Oceanogr. 48 (11), 2593–2607.
Uchida, T., Abernathey, R., Smith, S., 2017. Seasonality of eddy kinetic energy in an eddy permitting global climate model. Ocean Modell. 118, 41 – 58.
Vallis, G. K., 2006. Atmospheric and Oceanic Fluid Dynamics. Cambridge University.
Venaille, A., 2012. Bottom-trapped currents as statistical equilibrium states above topographic anomalies 699, 500–510.
Visbeck, M., Marshall, J., Haine, T., Spall, M., 1997. Specification of eddy transfer coefficients in coarse-resolution ocean circulation models. J. Phys. Oceanor. 27, 381–402.
Wang, D., Mooers, C. N. K., 1976. Coastal-trapped waves in a continuously stratified ocean. J. Phys. Oceanogr. 6 (6), 853–863.
Wang, Y., Stewart, A. L., 2018. Eddy dynamics over continental slopes under retrograde winds: Insights from a model inter-comparison. Ocean Modell. 121, 1 – 18.
Yang, L., Nikurashin, M., Hogg, A. M., Sloyan, B. M., 2018. Energy loss from transient eddies due to lee wave generation in the Southern Ocean. J. Phys. Oceanogr. 48 (12), 2867–2885.
Young, W. R., 2012. An exact Thickness-Weighted Average formulation of the Boussinesq equations. J. Phys. Oceanogr. 42 (5), 692–707.
Zhai, X., Greatbatch, R. J., 2007. Wind work in a model of the northwest Atlantic Ocean. Geophys. Res. Lett. 34 (4).
Zhang, W. G., Lentz, S. J., 2017. Wind-driven circulation in a shelf valley. Part I: Mechanism of the asymmetrical response to along-shelf winds in opposite directions. J. Phys. Oceanogr. 47 (12), 2927–2947.
Zhang, W. G., Lentz, S. J., 2018. Wind-driven circulation in a shelf valley. Part II: Dynamics of the along-valley velocity and transport. J. Phys. Oceanogr.

48 (4), 883–904.